Journal of Geophysical Research: Space Physics

RESEARCH ARTICLE
10.1029/2018JA025984

Key Points:
- MMS observed a burst of independent transverse EMIC waves with orthogonal linear polarizations following the shock
- Wave onsets at both MMS and Van Allen Probe A were consistent with theoretical expectations based on particle observations
- A rarely observed minimum in wave power at the gyrofrequency of He^{++} ions was present both before and after the shock

Correspondence to:
M. J. Engebretson,
engebret@augsburg.edu

Citation:
Engebretson, M. J., Posch, J. L., Capman, N. S. S., Campuzano, N. G., Bělik, P., Allen, R. C., et al. (2018). MMS, Van Allen Probes, GOES 13, and ground-based magnetometer observations of EMIC wave events before, during, and after a modest interplanetary shock. *Journal of Geophysical Research: Space Physics*, *123*, 8331–8357. https://doi.org/10.1029/2018JA025984

Received 9 AUG 2018
Accepted 26 SEP 2018
Accepted article online 29 SEP 2018
Published online 27 OCT 2018

MMS, Van Allen Probes, GOES 13, and Ground-Based Magnetometer Observations of EMIC Wave Events Before, During, and After a Modest Interplanetary Shock

M. J. Engebretson[1], J. L. Posch[1], N. S. S. Capman[1], N. G. Campuzano[1], P. Bělik[1], R. C. Allen[2], S. K. Vines[2], B. J. Anderson[2], S. Tian[3], C. A. Cattell[3], J. R. Wygant[3], S. A. Fuselier[4,5], M. R. Argall[6], M. R. Lessard[6], R. B. Torbert[4,6], M. B. Moldwin[7], M. D. Hartinger[8], H. Kim[9], C. T. Russell[10], C. A. Kletzing[11], G. D. Reeves[12], and H. J. Singer[13]

[1]Department of Physics, Augsburg University, Minneapolis, MN, USA, [2]Applied Physics Laboratory, The Johns Hopkins University, Laurel, MD, USA, [3]School of Physics and Astronomy, University of Minnesota, Twin Cities, Minneapolis, MN, USA, [4]Southwest Research Institute, San Antonio, TX, USA, [5]Department of Physics and Astronomy, University of Texas at San Antonio, San Antonio, TX, USA, [6]Space Science Center, University of New Hampshire, Durham, NH, USA, [7]Climate and Space Sciences and Engineering, University of Michigan, Ann Arbor, MI, USA, [8]Bradley Department of Electrical and Computer Engineering, Virginia Polytechnic Institute and State University, Blacksburg, VA, USA, [9]New Jersey Institute of Technology, Newark, NJ, USA, [10]Department of Earth, Planetary, and Space Sciences and Institute for Geophysics and Planetary Physics, UCLA, Los Angeles, CA, USA, [11]Department of Physics and Astronomy, University of Iowa, Iowa City, IA, USA, [12]Space Science and Applications Group, Los Alamos National Laboratory, Los Alamos, NM, USA, [13]NOAA Space Weather Prediction Center, Boulder, CO, USA

Abstract The stimulation of electromagnetic ion cyclotron (EMIC) waves by a magnetospheric compression is perhaps the closest thing to a controlled experiment that is currently possible in magnetospheric physics, in that one prominent factor that can increase wave growth acts at a well-defined time. We present a detailed analysis of EMIC waves observed in the outer dayside magnetosphere by the four Magnetosphere Multiscale (MMS) spacecraft, Van Allen Probe A, and GOES 13 and by four very high latitude ground magnetometer stations in the western hemisphere before, during, and after a modest interplanetary shock on 14 December 2015. Analysis shows several features consistent with current theory, as well as some unexpected features. During the most intense MMS wave burst, which began ~ 1 min after the end of a brief magnetosheath incursion, independent transverse EMIC waves with orthogonal linear polarizations appeared simultaneously at all four spacecraft. He^{++} band EMIC waves were observed by MMS inside the magnetosphere, whereas almost all previous studies of He^{++} band EMIC waves observed them only in the magnetosheath and magnetopause boundary layers. Transverse EMIC waves also appeared at Van Allen Probe A and GOES 13 very near the times when the magnetic field compression reached their locations, indicating that the compression lowered the instability threshold to allow for EMIC wave generation throughout the outer dayside magnetosphere. The timing of the EMIC waves at both MMS and Van Allen Probe A was consistent with theoretical expectations for EMIC instabilities based on characteristics of the proton distributions observed by instruments on these spacecraft.

1. Introduction

Electromagnetic ion cyclotron (EMIC) waves are one of several categories of ultra-low-frequency (ULF, 0.001–5.0 Hz) waves in Earth's magnetosphere. These waves can transfer energy between different plasma populations and precipitate energetic ions and electrons into the ionosphere and upper atmosphere. Numerous observational studies have confirmed the theoretical understanding originally presented by Cornwall (1965) and Kennel and Petschek (1966). In particular, for a distribution of ring current protons with pitch angle anisotropy A that exceeds the critical anisotropy, $A_c = \frac{1}{(\omega_p/\omega)-1}$, a cyclotron resonance can occur when the Doppler-shifted wave frequency ω equals the cyclotron frequency ω_p of the protons. This resonance causes wave growth and pitch angle scattering leading to the precipitation of a fraction of the protons into the ionosphere.

Cornwall et al. (1970) concluded on theoretical grounds that ion cyclotron instability for ring current protons exterior to the plasmapause was unlikely and that EMIC waves were most likely to occur in the region of overlap between the outer plasmasphere and the inner edge of the ring current. However, observations from high-altitude spacecraft beginning with Active Magnetosphere Particle Tracer Explorers Charge Composition Explorer (AMPTE CCE; Anderson et al., 1992) have shown that the occurrence probability of EMIC waves was in fact highest in the dayside magnetosphere well outside of the plasmapause. Subsequent observational studies have confirmed the AMPTE CCE results (e.g., Allen et al., 2015; Keika et al., 2013; Min et al., 2012; Usanova et al., 2012). In addition, Fraser and Nguyen (2001) and Tetrick et al. (2017) have shown that the plasmapause is not a strongly preferred source region for these waves, and compressions of the magnetosphere have been shown to be an effective trigger for the outer magnetosphere EMIC wave events (e.g., Allen et al., 2015, 2016; Anderson & Hamilton, 1993; Anderson, Erlandson, et al., 1996; Arnoldy et al., 1996; Fuselier et al., 2004; Tetrick et al., 2017; Usanova et al., 2012).

This paper presents observations of EMIC waves and associated ring current proton distributions associated with a rapid but short-lived magnetospheric compression near 1324 UT on 14 December 2015 and a subsequent continued increase in solar wind dynamic pressure, both associated with the passage of a modest interplanetary shock. It provides a detailed analysis of the timing and structure of the observed waves, including a comparison of the waveforms observed at the four closely-spaced MMS spacecraft, as well as an analysis of the instability of the proton distributions at both MMS and Van Allen Probe A. Section 2 introduces the sources of the wave and particle data, section 3 gives a detailed description of the wave and particle observations, and section 4 discusses the propagation and timing of the wave burst that occurred immediately after the peak of the initial compression. Section 5 presents a discussion of these observations, and our findings are summarized in section 6.

2. Instrumentation

The Magnetospheric Multiscale (MMS) mission consists of four closely-spaced (down to ~7 km) spacecraft in a highly elliptical, intermediate-inclination (28° geographic) orbit with apogee from 12 to 25 R_E (Burch et al., 2016; Fuselier et al., 2016). The spacecraft are spin stabilized with a spin period of 20 s. Each MMS spacecraft returns data in two general modes, survey and burst. The survey mode consists of *fast survey*, in which continuous data products are telemetered to the ground while MMS is in the mission's science *regions of interest*, and *slow survey* immediately before and after the regions of interest, in which most instruments transmit lower resolution data. Very high data rate *burst* products are produced only during fast survey mode, and only selected intervals of these data are transmitted to the ground.

Magnetic field measurements are provided by the MMS Fluxgate Magnetometer (FGM; Russell et al., 2016; Torbert et al., 2016). The MMS FGM data presented here were all obtained in slow survey mode, with a sampling rate of 8/s, and are presented after rotation into local field-aligned coordinates, with components Bx and By oriented transverse to the local field and radially outward and eastward, respectively, and component Bz along the direction of the field.

Electric field measurements presented here are provided by the Spin-Plane Double Probe (SDP) instrument, consisting of four spherical electrodes at the end of 60 m wire booms (Lindqvist et al., 2016), and the Axial Double Probe (ADP) instrument consisting of two electrodes separated by ~ 29.2 m in effective antenna length (Ergun et al., 2016). DC vector electric field data were also obtained in slow survey mode, with a sampling rate of 8 Hz (Torbert et al., 2016).

Ion composition data from MMS were obtained by the Hot Plasma Composition Analyzer (HPCA), which measures fluxes of H^+, He^{++}, He^+, and O^+ in the energy range from 1 eV/e to 40 keV/e (Young et al., 2016). A complete set of measurements is made every 10 s (every half spin of the spacecraft). HPCA data presented here were also obtained in slow survey mode, in which one 10-s snapshot of the distribution function for H^+ and heavier ions from 1 eV to 40 keV in 16 energies was obtained every 70 s.

The Van Allen Probes consist of two identically instrumented spacecraft with apogees of 5.8 R_E, perigee ~ 600 km, and an orbital period of 9 hr. Their near-equatorial orbits are inclined 10° with respect to the equator, enabling nominal sampling to magnetic latitudes of 0° ± 21° (Mauk et al., 2013). Magnetometer data used in this study were obtained by the EMFISIS (Electric and Magnetic Field Instrument Suite and Integrated Science)

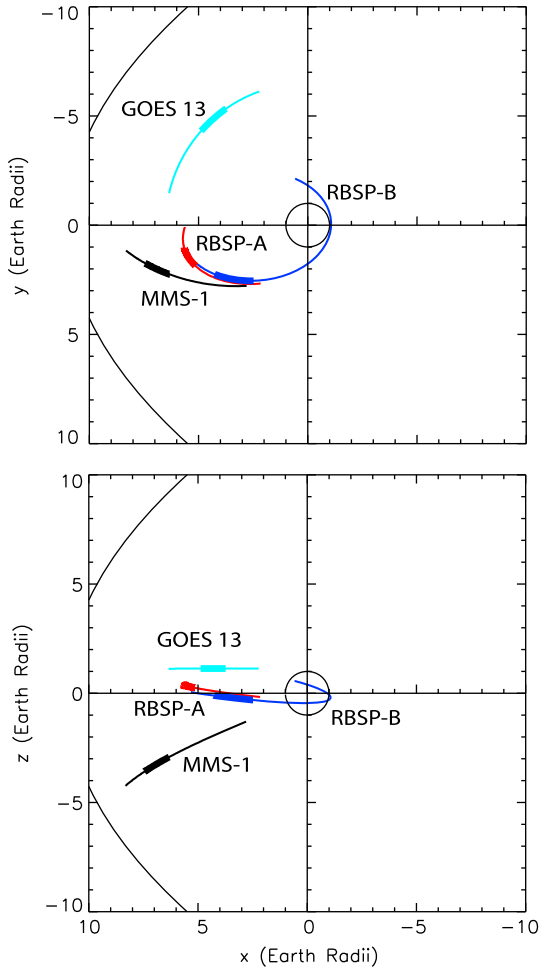

Figure 1. Segments of the orbits of MMS 1 (black), Van Allen Probes A (red) and B (dark blue), all traveling inbound, and GOES 13 (light blue), shortly after local noon between 1200 and 1600 UT on 14 December 2015, in the SM (solar magnetic coordinate system) *XY* and *XZ* planes. The interval between 1300 and 1400 UT is indicated by thicker lines. The Sun is to the left.

instrument package, which measures vector magnetic fields at a cadence of 64 vector samples/s, for a Nyquist rate of 32 Hz (Kletzing et al., 2013).

Energetic ions and electrons were measured using several instruments. As part of the Energetic Particle, Composition, and Thermal Plasma (ECT) suite (Spence et al., 2013) ions with energies from 1 eV or spacecraft potential (whichever is greater) to 50 keV were measured by the ECT/HOPE (Helium Oxygen Proton Electron) mass spectrometer instrument (Funsten et al., 2013).

EMIC wave activity at GOES 13, in geostationary orbit at 6.6 R_E, was measured by the vector fluxgate magnetometer (Singer et al., 1996). Data were sampled at a 0.512-s cadence, for a Nyquist frequency of 0.976 Hz.

Figure 1 shows segments of the orbits of MMS 1 and Van Allen Probes A and B, all traveling inbound shortly after local noon between 1200 and 1600 UT on 14 December 2015, as well as GOES 13, located in the prenoon local time sector. Figure 2 shows the SSCWEB-based northern hemisphere foot points of the magnetic field lines traversed by these spacecraft.

Also shown in Figure 2 are the locations of two high-latitude ground-based magnetometers in the northern hemisphere and the magnetic conjugate foot points of two high-latitude ground-based magnetometers in Antarctica, all located close to but somewhat west of the magnetic footpoint of MMS during the interval between 1300 and 1400 UT. Each of these instruments has sufficient sensitivity and a high enough sampling rate to detect EMIC waves. The two northern hemisphere stations include a Narod fluxgate magnetometer at Pangnitung, Canada, part of the Magnetometer Array for Cusp and Cleft Studies (MACCS; Engebretson et al., 1995) and an induction coil (search coil) magnetometer at Sondrestromfjord, Greenland, part of the Magnetic Induction Coil Array (MICA; Kim et al., 2017). The two Antarctic stations include an additional MICA instrument at South Pole Station, and an induction coil magnetometer (AAL-PIP PG3) that is part of the Autonomous Adaptive Low-Power Instrument Platform array (Clauer et al., 2014). Table 1 lists the geographic coordinates, corrected geomagnetic coordinates, and nominal L shell for each of these stations (based on the IGRF magnetic field model for epoch 2015).

3. Satellite Observations

Cattell et al. (2017) documented the impact of the modest interplanetary shock that was observed upstream of Earth by ACE at 1231 UT and by Wind at 1241 UT. The shock compressed the dayside magnetopause to inside 8 R_E. Figure 3a shows the Z (north-south) component of the interplanetary magnetic field, Figure 3b shows the solar wind flow pressure P_{sw}, Figure 3c shows the AE index, and Figure 3d shows the SYM-H index from 1200 to 1600 UT. A southward turning of the interplanetary magnetic field coincided with an increase of P_{sw} from 2 to 5 nPa from 1320 to 1330 UT.

The resulting compression of the magnetosphere caused an inward excursion of the magnetopause past the orbit of the four MMS spacecraft. Figure 3e, a Fourier spectrogram of the azimuthal By component of MMS 1 magnetometer data, shows a roughly 2-min interval of intense broadband noise at 1324 UT, and Figure 3f shows the Z_{GSM} component of the DC magnetic field, which during this same interval recorded a southward magnetic field. Both of these are evidence that for this short interval MMS 1 was outside the magnetopause and in the magnetosheath.

The compression of the dayside magnetosphere caused the total magnetic field (not shown) to increase from 80 to 125 nT at MMS 1, from 160 to 185 nT at Van Allen Probe A, and from 113 to 127 nT at GOES 13. A continued but irregular increase in solar wind flow pressure persisted until nearly 1600 UT.

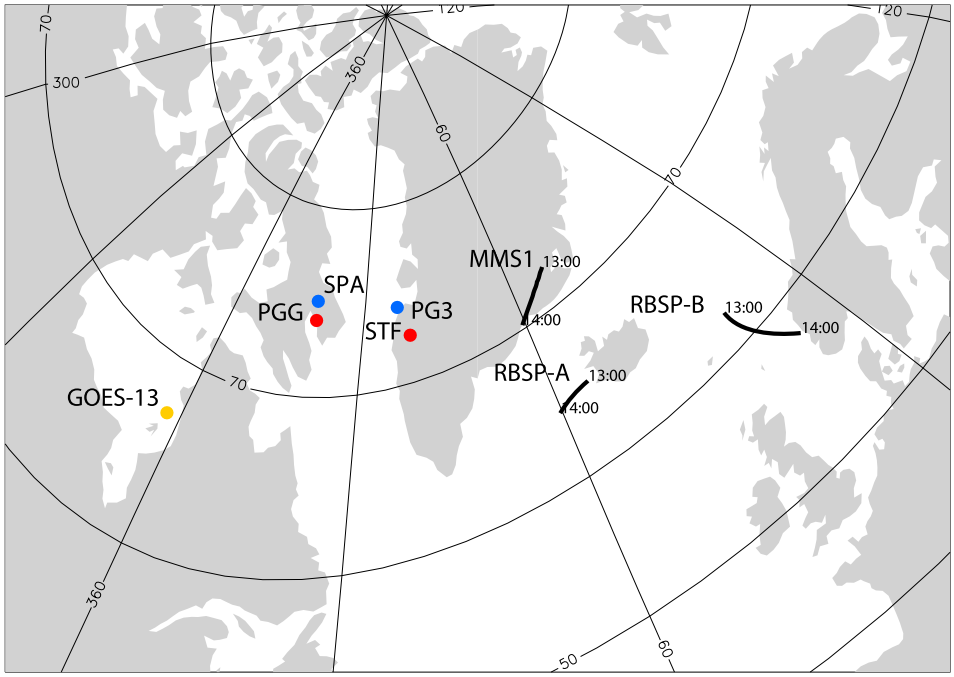

Figure 2. The black lines show the northern hemisphere foot points of the magnetic field lines traversed by MMS 1 and Van Allen Probes A and -B between 1300 and 1400 UT on 14 December 2015, and the orange dot shows the northern hemisphere footpoint of GOES-13. The red dots indicate the locations of northern hemisphere ground magnetometers at Sondrestromfjord, Greenland (STF) and Pangnirtung, Canada (PGG); the blue dots indicate the northern hemisphere locations conjugate to South Pole Station (SPA) and AAL-PIP station PG3 in Antarctica.

Figure 4 shows simultaneous Fourier spectrograms of differenced magnetic field data from MMS 1, Van Allen Probe A, GOES 13, AAL-PIP station PG3 (Antarctica), and Sondrestromfjord (Greenland) during this same interval, from 1200 to 1600 UT. Some EMIC wave activity was observed before the 1324 UT compression event at MMS 1, GOES 13, and the ground stations, and numerous intervals of wave activity were observed for most of the next 2 hr at all five locations. Most of the wave activity observed by spacecraft was in the hydrogen band (between the He^+ and H^+ gyrofrequencies), but some helium band activity was observed by MMS 1 and Van Allen Probe A as they traveled inbound to lower L shells. A relative minimum in wave power at the He^{++} gyrofrequency is also evident in the MMS spectrogram during most wave events. Van Allen Probe B was located near L = 4.4 at the time of the compression and observed no wave activity between 1300 and 1400 UT. Cattell et al. (2017) noted that the number density of plasma ranged from ~10 to 30 cm^{-3} on Probe A and ~100 to 120/cm^3 on Probe B, consistent with Probe A being located outside or near the plasmapause, while Probe B was located within the plasmasphere.

Table 1
Ground-Based Magnetometer Stations With Data Used in This Study

Station	Array	Geog. Lat.	Geog. Lon.	CGM Lat.	CGM Lon.	L shell
Northern Hemisphere Stations						
Pangnirtung	MACCS	66.1	294.2	73.4	19.6	12.4
Sondrestromfjord	MICA	67.0	309.3	72.0	39.6	10.6
Antarctic Stations						
South Pole	MICA	−90.0	--	−74.4	18.8	14.1
PG3	AAL-PIP	−84.8	37.63	−73.8	36.8	13.0

Note. Corrected geomagnetic (CGM) coordinates were calculated using VITMO ModelWeb, https://omniweb.gsfc.nasa.gov/vitmo/cgm_vitmo.html, for epoch 2015.

3.1. EMIC Waves Observed by MMS

Panels a, b, and c of Figure 5 show all three components of the EMIC wave activity observed by the MMS 1 FGM instrument between 1300 and 1400 UT. Also shown are the ellipticity of the waves (panel d) and the wave normal angle (panel e), calculated using the method of Means (1972). Pixels in panels d and e are colored black for all cases when the wave power in Bx was below 10^{-6} nT^2-Hz. Nearly identical spectrograms were obtained using data from MMS 2, 3, and 4 (not shown).

Wave activity before the magnetosheath incursion (between 1323:30 and 1325:15 UT) included a 500 mHz purely compressional narrowband emission (appearing only in the Bz component; panel c) from 1235 (not shown) to 1312 UT and two intervals of transverse emissions from 1304 to 1312 (400 mHz, predominantly transverse) and 1313 to 1322 UT (450 mHz,

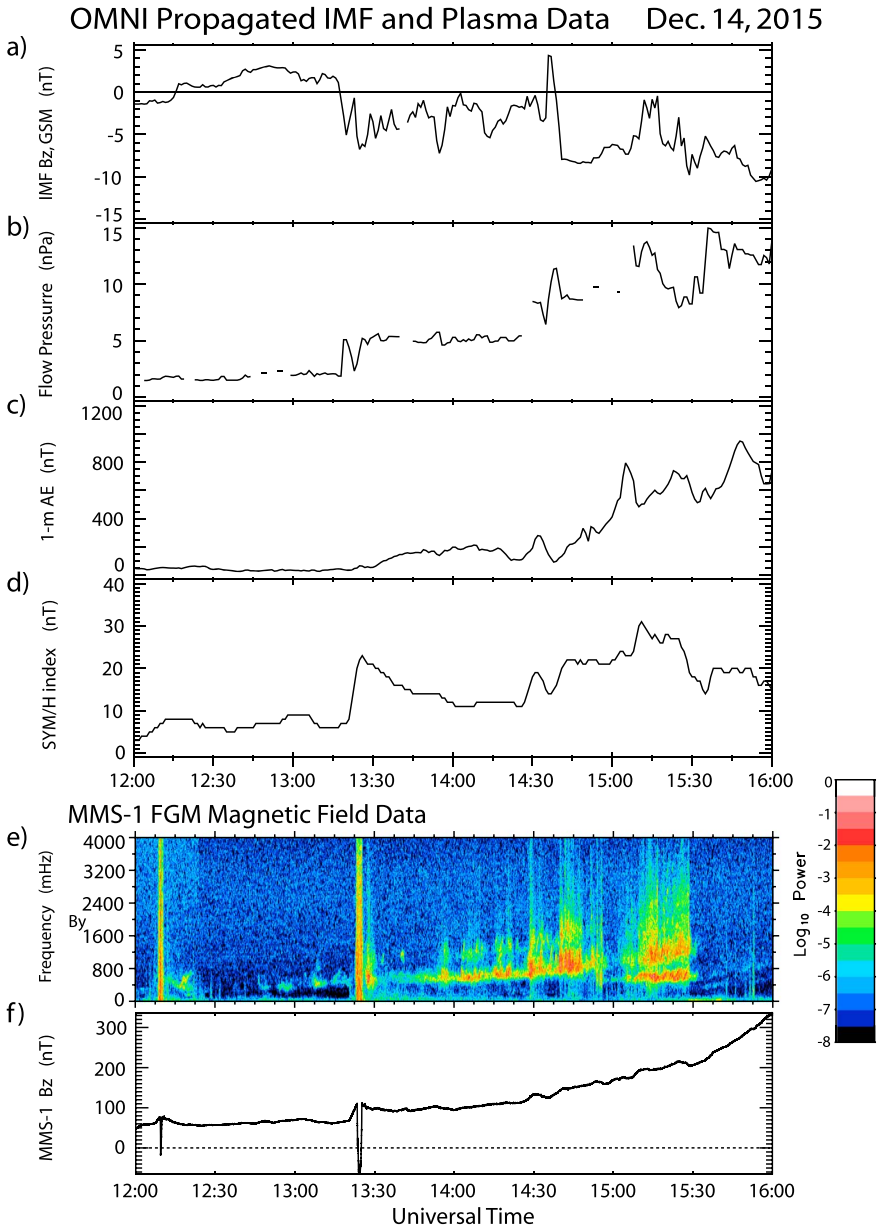

Figure 3. (a–d) Data from the OMNI database from 1200 to 1600 UT on 14 December 2015. Panel a shows the north-south component of the interplanetary magnetic field (Bz) and panel b the solar wind flow pressure (Psw), both propagated in time to the bow shock. Panel c shows the 1-min AE index, and panel d the 1-min SYM-H index. Panel e is a Fourier spectrogram of the transverse azimuthal component (By) of differenced magnetic field data from MMS 1 after rotation into field-aligned coordinates, and panel f shows the north-south component of the MMS 1 magnetic field (Bz) in GSM coordinates.

purely transverse). The transverse emissions had mixed but mostly linear polarization, and a wave normal angle near 0°. The wave normal angle near 90° at 1307 UT was associated with low-amplitude 500 mHz waves, apparently due to a mixture of transverse and compressional waves.

Between 1326 and 1327 UT, immediately after the magnetopause moved outward again past the MMS spacecraft, some moderate-amplitude diffuse, primarily compressional wave activity appeared, with power strongest in the Bz component near 600 mHz and wave normal angle near 90°. This was immediately followed by an intense primarily transverse wave burst with frequency between 300 and 800 mHz, with mixed but primarily linear polarization, and with wave normal angle near 0°, between 1327 and 1331 UT. Two shorter, higher frequency wave bursts appeared near 1332 and 1340 UT. Both were primarily left-hand

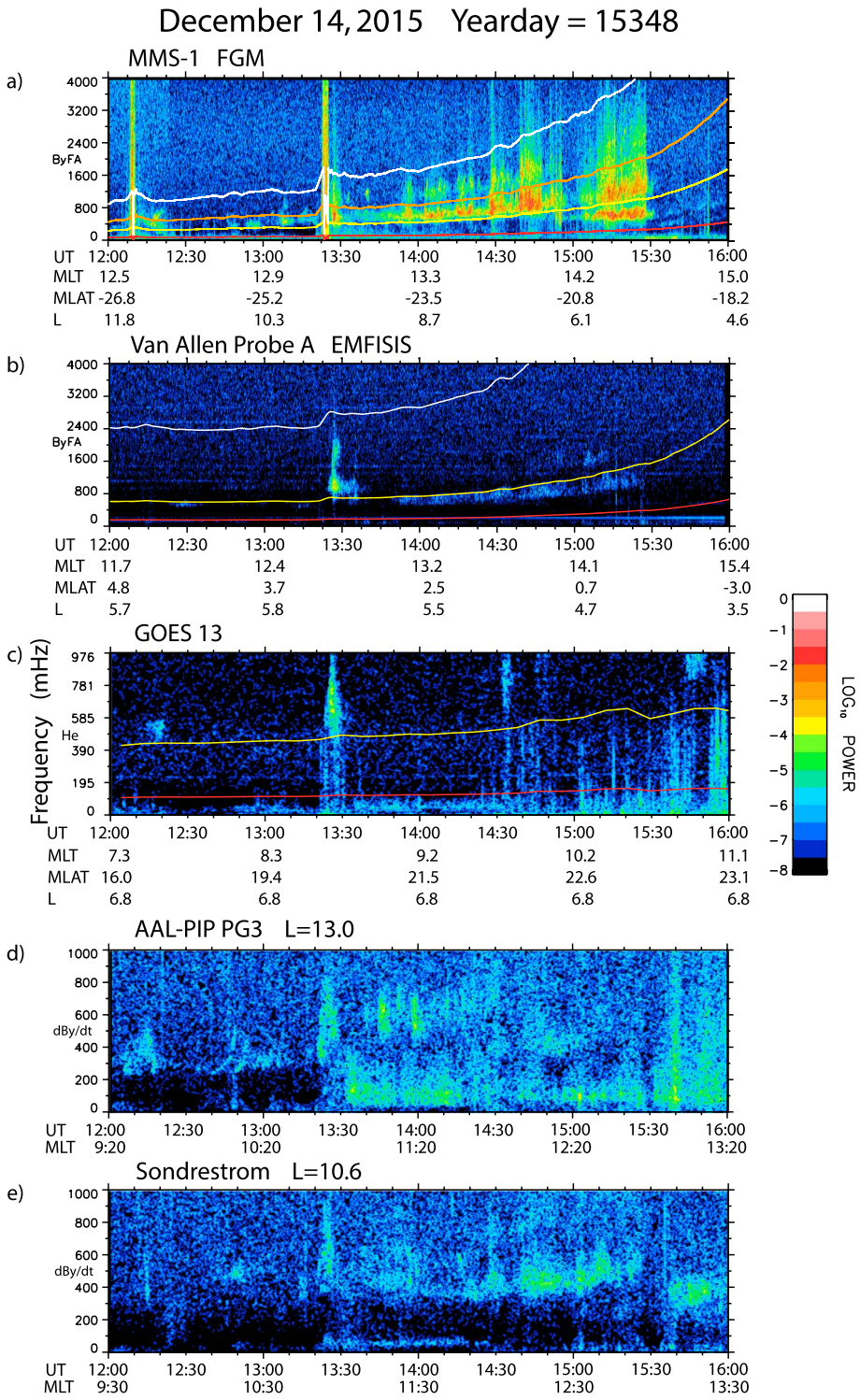

Figure 4. Fourier spectrograms of differenced magnetic field data from MMS 1, Van Allen Probe A, GOES 13, AAL-PIP PG3, and Sondrestrom, Greenland, from 12:00 to 16:00 UT on 14 December 2015. Panels a and b show the transverse azimuthal component of satellite fluxgate magnetometer data rotated into field-aligned coordinates, panel c shows the radial (He) component of satellite fluxgate magnetometer data, and panels d and e show the east-west (dBy/dt) component of ground-based search coil magnetometer data. The white, orange, yellow, and red curves in panels a, b, and c show the H^+, He^{++}, He^+, and O^+ gyrofrequencies, and the constant-frequency blue line slightly below 0.2 Hz in panel b is a subharmonic of the Van Allen Probe A spin frequency.

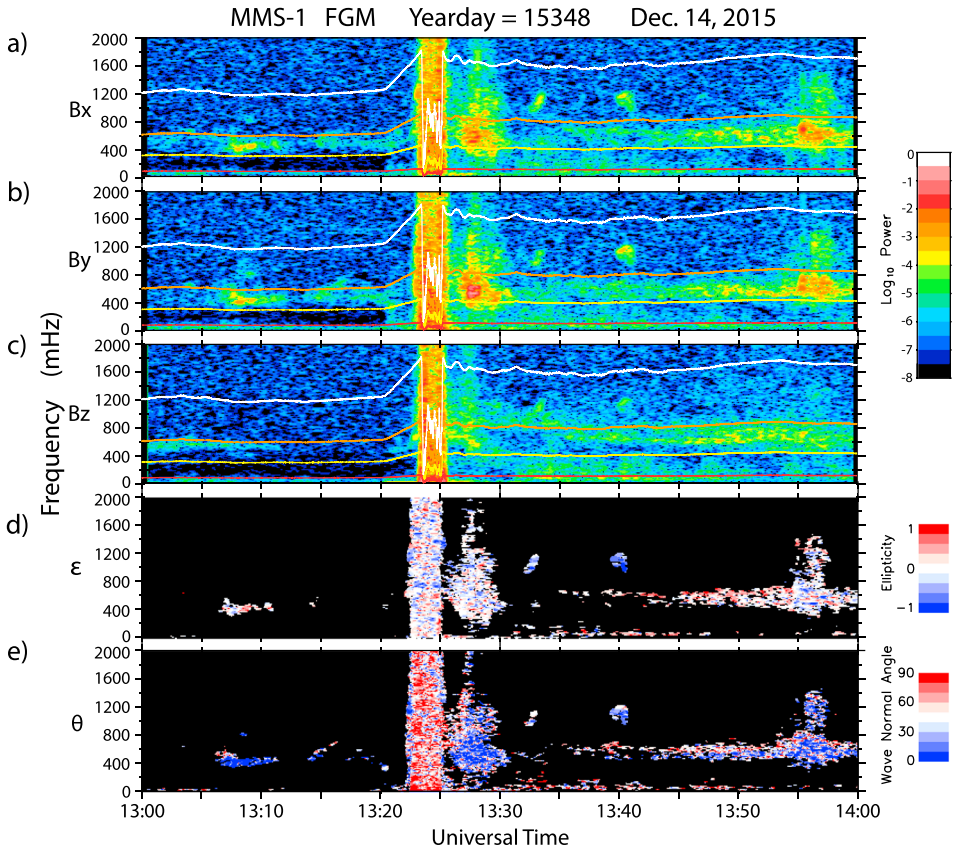

Figure 5. Fourier spectrograms of differenced magnetic field data from MMS 1 from 1300 to 1400 UT on 14 December 2015. (a–c) The wave power as a function of frequency (in mHz) in local field-aligned coordinates (Bx radial, By azimuthal, and Bz parallel to the total field), respectively. Panel d shows the ellipticity (−1 for left-handed circularly polarized, 0 for linearly polarized, and +1 for right-handed circularly polarized), and panel e shows the wave normal angle. The white, orange, yellow, and red lines in panels a–c show the H^+, He^{++}, He^+, and O^+ gyrofrequencies.

polarized, with wave normal angle near 0°. Weak ~900 mHz compressional wave power appeared in the Bz component from1330 to 1335, and a nearly continuous ~500 mHz wave train with gradually increasing amplitude and occasional primarily transverse bursts and nearly equal power in all three components began near 1335 UT and continued, with gradually increasing frequency, until 1450 UT (cf. Figure 4). This wave train again had mixed polarization and a mixture of wave normal angles.

Figure 6 supplements Figure 5 by showing Fourier spectrograms of total wave power of both the magnetic field **B** (panel a) and the electric field **E** (panel b), as well information about the Poynting vector **S** (panels c–g). Panel c shows the magnitude of **S**, panel d shows the angle between **S** and **B**, and panels e–g show the *X*, *Y*, and *Z* components of **S** in a local field-aligned coordinate system. Panels d–g only show results for times and frequencies with $|\mathbf{S}| > 9 \times 10^{-3}$ W/km^2 (panel c).

The purely compressional 500 mHz waves before 1312 UT and the 900 mHz compressional waves between 1330 and 1335 were accompanied by negligible Poynting vector amplitude. All of the transverse wave events shown in Figure 5, however, had significant Poynting amplitude, and the direction of **S** exhibited significant differences between events. Panel d shows that during the transverse 400 mHz wave packet observed between 1304 and 1312 UT, the angle between **S** and **B** was initially near 180° (red) between 1307 and 1308 UT, and hence, antiparallel to **B** and directed southward away from the equator, but between 1308 and 1310 UT was near 0° (blue), parallel to **B**, and thus directed northward toward the equator.

The much stronger Poynting vector during the 300–800 mHz predominantly transverse emission between 1327 and 1331 UT was directed predominantly southward away from the equator (panels d and g), but two wave bursts shown in red in panel c (intensifications in the compressional component) coincided with

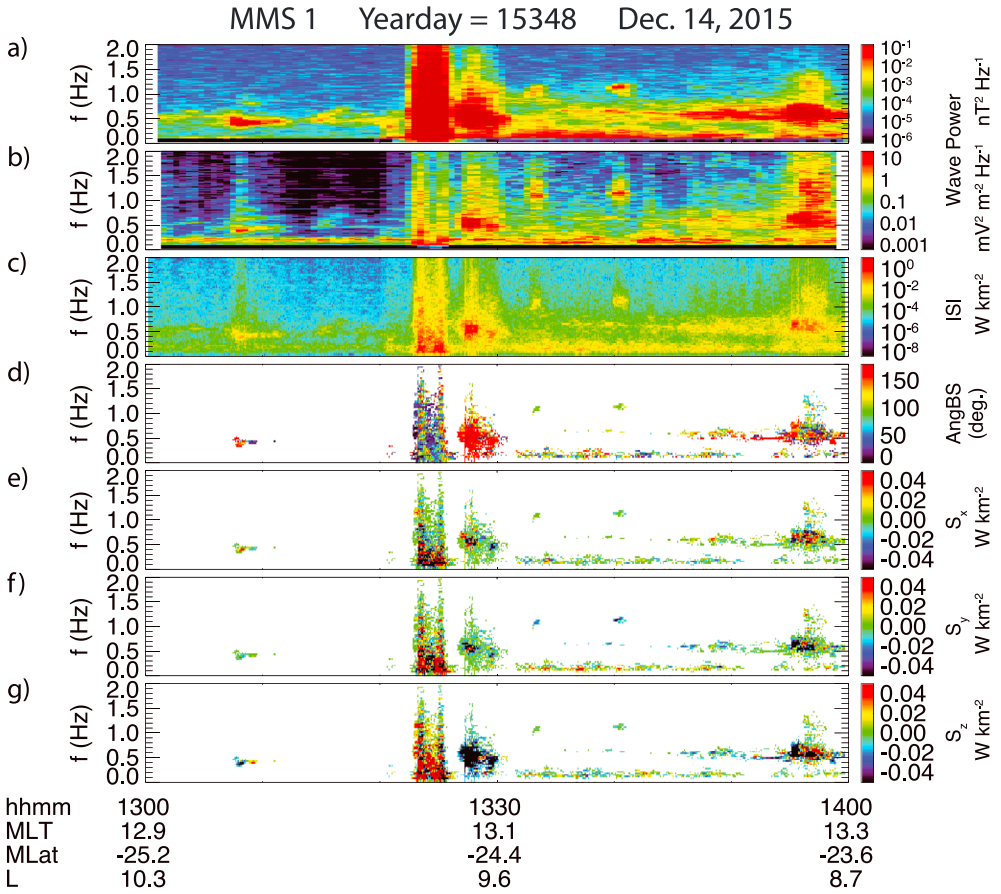

Figure 6. Frequency versus time spectrograms from 1300 to 1400 UT on 14 December 2015 of total wave power in (a) the magnetic field B, (b) the electric field E, and (c) the magnitude of the Poynting vector S. (d) The angle between the Poynting vector and the background magnetic field. (e) The components of the Poynting flux S in the field-aligned coordinate *X*, *Y*, and *Z* directions.

intervals of enhanced Sx and Sy (panels e and f). The complexity of these signals is explored in more detail below. During the two short higher frequency wave bursts near 1332 and 1340 UT, **S** was directed obliquely, in the azimuthal (*y*) direction. During the extended interval of transverse 500 mHz wave activity beginning at 1335 and extending to 1350 UT, **S** was again directed predominantly southward, but again with some intervals with increased compressional components directed obliquely.

Figures 7–10 provide more detailed views of two intervals of this wave activity, again in local field-aligned coordinates. Figure 7 shows a 1-min interval of 0.4–2.0 Hz band-pass-filtered wave activity in all three magnetic field components at MMS 1 during the intense wave burst between 1327 and 1331 UT, using a uniform vertical scale. Panel a shows a series of short quasi-sinusoidal wave packets in the Bx component, separated by lower amplitude signals and phase shifts. Considerably larger amplitude wave packets were observed in the By component (panel b), again separated by intervals of lower amplitude and phase shifts. Waves in the Bz component (panel c) were much weaker, with few clear wave packets but again with multiple phase shifts, and the wave packets in each of the three components appeared to be largely independent of those in the other components; the transverse waves in Bx and By were thus linearly polarized.

Panels a and b of Figure 8 show the Bx (transverse radial) and By (transverse azimuthal) components of the magnetic field at all four MMS spacecraft, respectively, again after band-pass filtering between 0.4 and 2.0 Hz. Signals from the four spacecraft are offset by 3 nT in the vertical direction for the *x* component and 10 nT for the *y* component. Panels c and d show the corresponding wave periods of the Bx and By components, respectively, at each of the four spacecraft. The precision of the period values is limited by the 0.125-s sampling rate of the data.

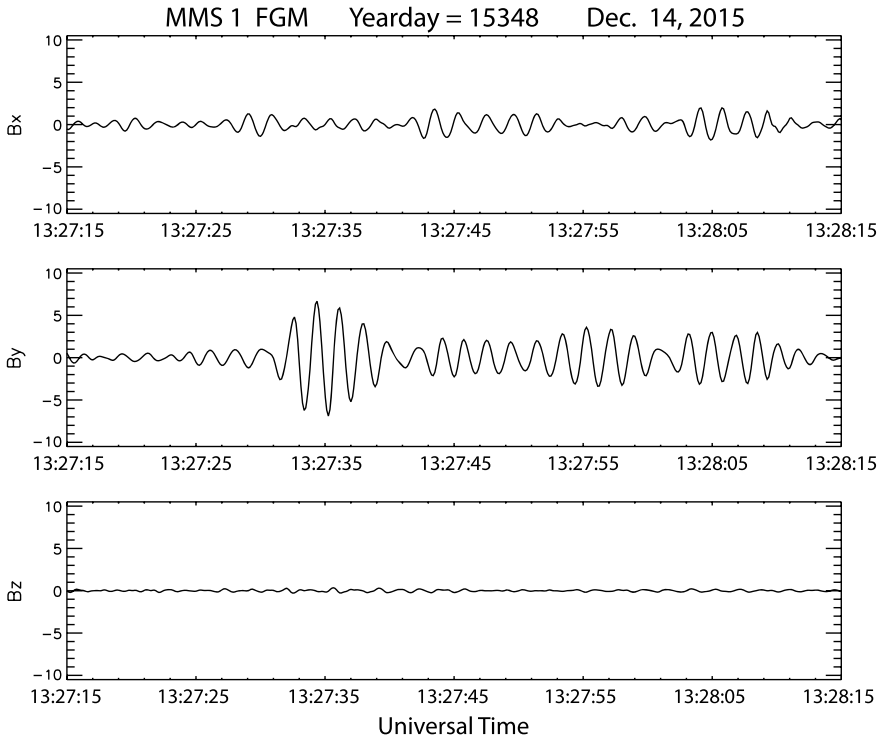

Figure 7. Three-axis plot of MMS 1 magnetic field data rotated into local field-aligned coordinates and band-pass filtered from 0.4 to 2.0 Hz, with uniform scale, from 1327:15 to 1328:15 UT on 14 December 2015.

Figure 8a shows that the wave signals in the Bx component were very similar at all four spacecraft. Comparison of Figures 8a and 8c shows that the phase shifts in the Bx component corresponded to jumps in the wave period that were often but not always of similar amplitude and sign at all four spacecraft. Comparison of Figures 8b and 8d shows the same pattern for the By component: clear phase shifts corresponded to jumps in the wave period. The red lines in Figures 8c and 8d help show that at all four spacecraft the period of the Bx component wave packets was centered near 1.75 s; the By period was slightly higher, near 2.0 Hz. A plot of the Bz wave periods showed few wave periods above 1 s, suggesting interference between multiple waves (not shown).

Figure 9 shows a plot of MMS 1 magnetic field data during the higher-frequency wave burst between 1340 and 1341 UT, after band-pass filtering between 0.8 and 2.0 Hz. The transverse components (Figures 9a and 9b) were composed of sinusoidal waves with few evident phase shifts, but the amplitude modulation suggests the apparent presence of wave packet structure. Hodogram analysis of this interval (not shown) indicated consistently left handed polarization during intervals with no phase jumps. The compressional component (Figure 9c) was a much more complex time series, with few clear wave packets and multiple phase shifts.

Figure 10, in a format similar to Figure 8, shows that the transverse waveforms (Figures 10a and 10b) were again very similar at all four spacecraft. Figures 10c and 10d show that the periods were constant at 0.875 s (to within the 0.125-s sampling rate) in both Bx and By at all four spacecraft except for two times in the Bx component: 1340:37 and 1340:54, each corresponding to phase shifts. Line spectra of unfiltered data (not shown) indicate the presence of two closely-spaced peaks in frequency, near 1.15 Hz (stronger) and 1.05 Hz (weaker), as well as a somewhat weaker signal near 0.63 Hz. The ~10-s period of wave packets and phase shifts evident in both components in Figure 10 is consistent with beating of the 1.15 Hz and 1.05 Hz signals and was reproduced in plots of synthetic data (not shown). Similar waveform plots of the compressional component were again very similar at all four spacecraft, and again during only two times near the end of the interval did the periods differ from 0.875 s by more than 0.125 s (not shown).

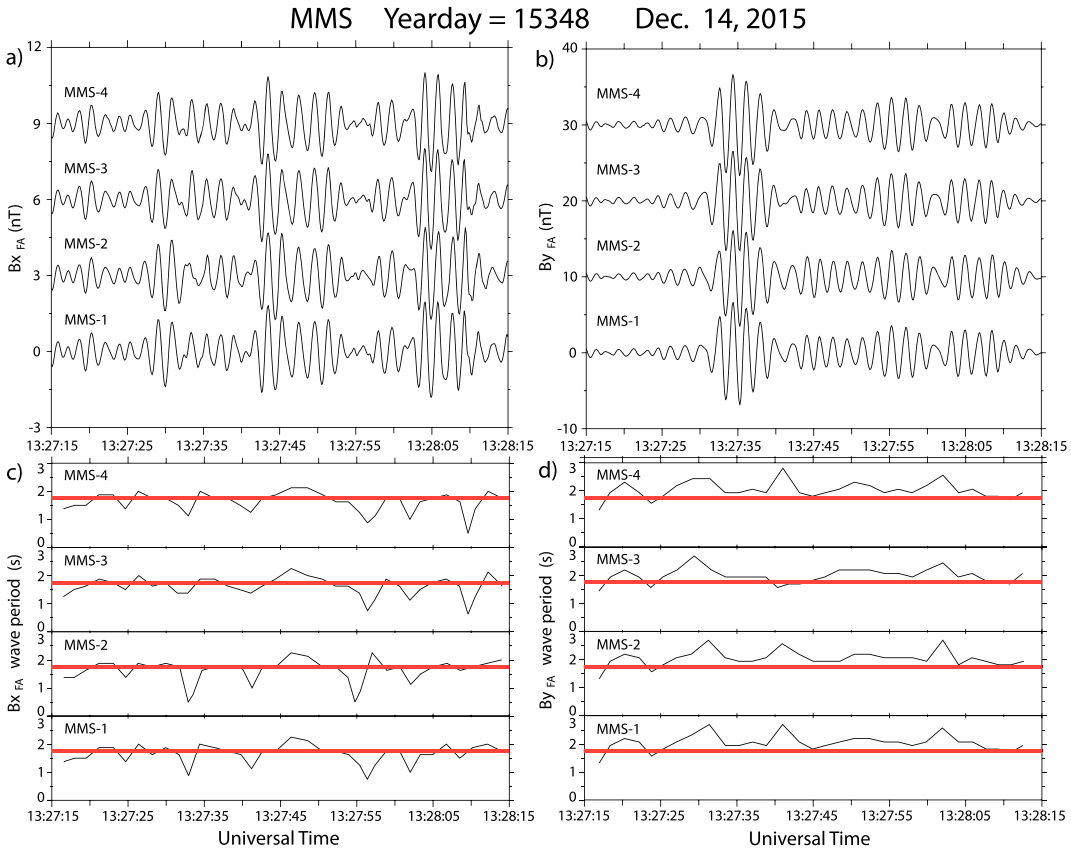

Figure 8. Waveforms and wave periods of electromagnetic ion cyclotron waves observed by the four MMS spacecraft between 1327:15 and 1328:15 UT on 14 December 2015. A band-pass filter between 0.4 and 2.0 Hz has been applied to the FGM data. (a and b) The Bx (transverse radial) and By (transverse azimuthal) components of the magnetic field in local field-aligned coordinates, respectively, offset by 3 and 10 nT in the vertical direction. (c and d) The corresponding wave periods of the Bx and By components, respectively, at each of the four spacecraft. The shaded lines are drawn at 1.75 Hz in panels c and d.

The complex nature of EMIC wave structures has been noted for many years. The presence of multiple EMIC wave packets has been shown by Denton et al. (1996); Anderson, Denton, and Fuselier (1996); and Remya et al. (2017) to affect the wave properties inferred from Fourier-based polarization analysis techniques. The information presented in Figures 9 and 10 confirms that for relatively simple waveforms (one or very few wave packets, as observed between 1340 and 1341 UT) detailed analyses are consistent with the Fourier-based ellipticity values shown in Figure 5, but for the waves observed between 1327:15 and 1328:15, the mixed ellipticity shown in Figure 5 does not accurately capture the detailed wave characteristics shown in Figures 7 and 8. Figures 7 and 8 clearly show the superposition of two temporally independent waves linearly polarized in the transverse azimuthal and radial directions (in a local field-aligned coordinate system).

Plots similar to Figures 7–10 were also generated for two other intervals (not shown). Between 1307 and 1310 UT short wave packets with periods of ~2 s or less and separated by numerous phase shifts appeared in the Bz component. Wave trains in the Bx and By components showed some similarities, were of longer duration between phase shifts, and consistently had periods of ~2.5 s. The waves in each component were very similar at all four spacecraft. Between 1356 and 1358 UT wave packets in the three magnetic field components were largely independent and many phase shifts appeared, and again, the waves in each component were very similar at all four spacecraft.

3.2. Ion Observations at MMS and EMIC Instability

In an extension of the earlier EMIC instability theory of Kennel and Petschek (1966), which focused on the proton anisotropy, Gary et al. (1994), using linear theory, one-dimensional hybrid simulations, and data analysis, found that EMIC waves created an upper bound on the hot proton temperature anisotropy, which varied

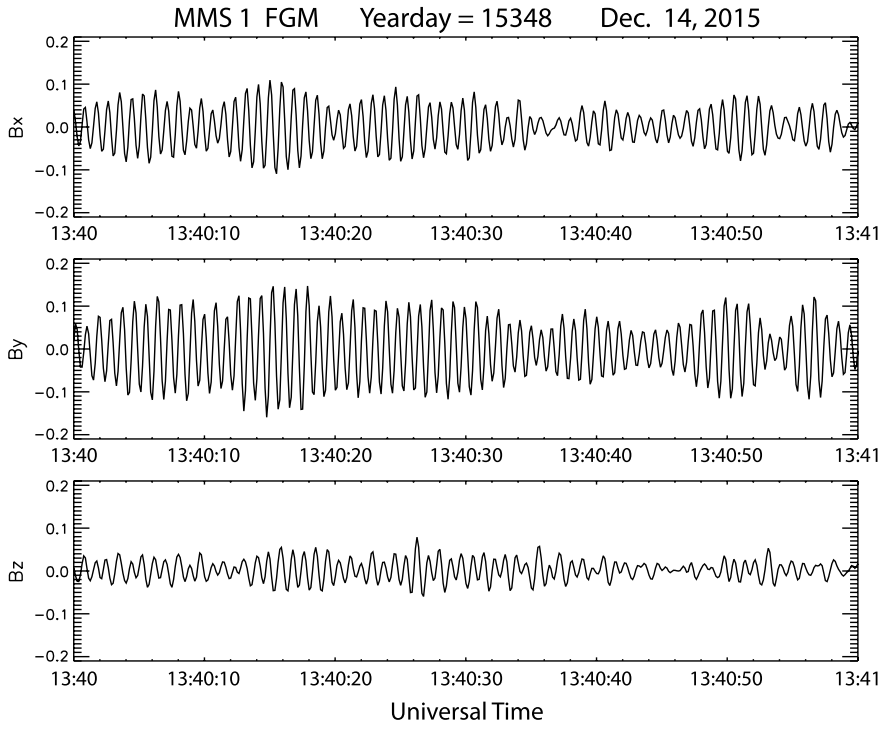

Figure 9. Three-axis plot of MMS 1 magnetic field data rotated into local field-aligned coordinates and band-pass filtered from 0.8 to 2.0 Hz, with uniform scale, from 1340 to 1341 UT on 14 December 2015.

inversely with the parallel plasma beta of the hot protons and was parameterized by the relative density of the hot component (n_h/n_e). Gary et al. (1994) verified this dependence using energetic particle data from the Los Alamos magnetospheric plasma analyzer in geosynchronous orbit. Anderson, Denton, Ho, et al. (1996) confirmed this relation using 24 intervals of EMIC wave activity (active) and 24 intervals with no EMIC waves (quiet) in the outer magnetosphere (L $>$ 7) observed by the AMPTE/CCE spacecraft, half of each in the dawn and noon local time sectors. They found that dawn intervals with EMIC waves displayed instability in 9 of 12 cases, whereas noon intervals required additional cold ion density (not measured well with AMPTE CCE) in order to yield instability in 10 of 12 cases. Intervals without EMIC waves all remained stable even with an additional 10/cm^3 of cold ions.

Blum et al. (2009) developed a proxy for EMIC wave instability based on these relationships and used it in a statistical study of EMIC wave growth during magnetic storms. The experimental instability parameter $\Sigma_h = \left(\frac{T_{\perp h}}{T_{\parallel h}} - 1\right)\beta_{\parallel h}^{\alpha_h}$, where $T_{\perp h}$ is the temperature of the component of hot protons (defined as having energies from 100 eV to 45 keV) perpendicular to B, $T_{\parallel h}$ is the temperature of the component of hot protons parallel to **B**, and $\beta_{\parallel h}$ is the hot beta parallel to **B**. This parameter can be compared to S_h, a parameter defined similarly to Σ_h but derived from linear theory assuming a threshold growth rate $\gamma_m/\Omega_p = 10^{-3}$. Both S_h and α_h are functions of the fractional hot proton density n_h/n_e, where n_h is the number density of hot protons and n_e is the total number density of electrons in the plasma.

In this section we present MMS particle data that are consistent with these earlier results and provide further insight into the wave observations. Figure 11 presents MMS 2 magnetic field and HPCA observations during the same interval from 1300 to 1400 UT shown in Figures 5 and 6. Panel a is a plot of the GSM magnetic field components and total field (Bx, By, Bz, and Btot), and panel b is an energy spectrogram of the omnidirectional differential fluxes of protons. Increased fluxes of protons with energies between 3 and 25 keV are evident throughout this interval.

Further details of the time dependence of the proton population and its angular distribution are shown in panels c–g. Panel c shows that the total flux in the magnetosphere is dominated by the lowest energy

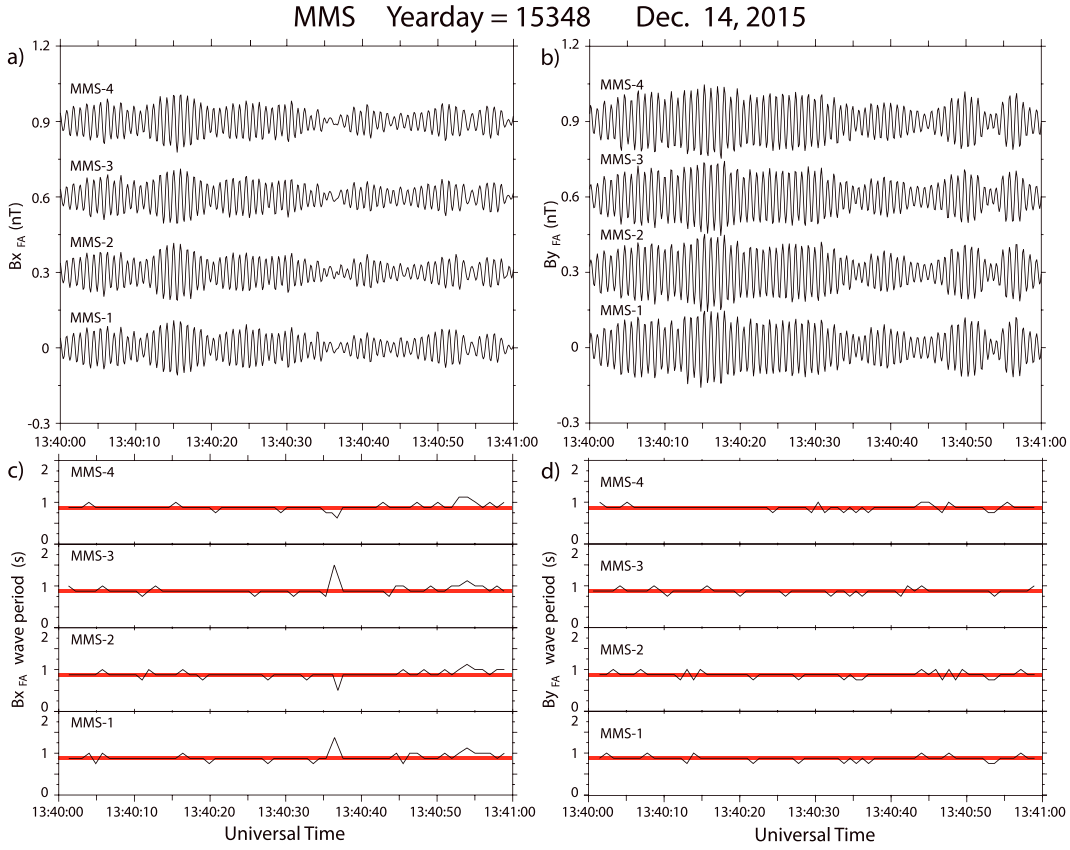

Figure 10. Waveforms and wave periods of electromagnetic ion cyclotron waves observed by the four MMS spacecraft between 1340 and 1341 UT on 14 December 2015, as in Figure 8. A band-pass filter between 0.8 and 2.0 Hz has been applied to the FGM data.

population, with energy below 0.1 keV. In particular, increased fluxes of these protons appeared between 1321 and 1323 UT (immediately before the magnetosheath intrusion) and between 1325:30 and 1330 UT (immediately after the magnetosheath intrusion, and including the time of the strongest EMIC wave burst). Panels f and g show that the fluxes with energies above 2 keV were strongly peaked near 90°, leading to large values of pitch angle anisotropy.

Panels h and i of Figure 11 not only document the presence of He^{++} ions with a broad range of energies in the magnetosheath (1323–1325 UT) but also a He^{++} population with energies above 10 keV in the magnetosphere. The pitch angle distribution of these ions was broadly peaked near 90°, and their flux was most intense immediately after the magnetosheath intrusion, from 1325 to ~1342 UT (panel i).

Proton contamination can be a problem for HPCA observations in certain regions; however, for this interval, the He^{++} signals at energies $>$10 keV/e are not a consequence of the protons at those energies. The proton flux at energies $>$10 keV/e are not high enough to cause any significant bleed-over into the He^{++} mass/charge range in the instrument. One indication that there is not significant proton contamination at these energies is that the pitch angle spectrograms for the same energy range (10–40 keV/e) are not the same between the two species throughout the hour shown in Figure 11 (panels g and panel i for protons and He^{++}, respectively). Also, seeing low fluxes of He^{++} in the outer magnetosphere at thermal to suprathermal energies (tens of keV) is quite common: He^{++} has been observed in the magnetosphere at low levels (a few percent of the proton population at the same energies) since at least 1980 (e.g., Ipavich and Scholer, 1983). A recent example of when there is both a real He^{++} population at tens of keV in the outer magnetosphere, as well as clear proton contamination in the other species observed by HPCA, can be found in Figure 2 of Vines et al. (2017): the contamination signatures were in the magnetosheath, where the bulk density was nearly 50/cm^3, well above that for this event. Thus, while the He^{++} population shows somewhat

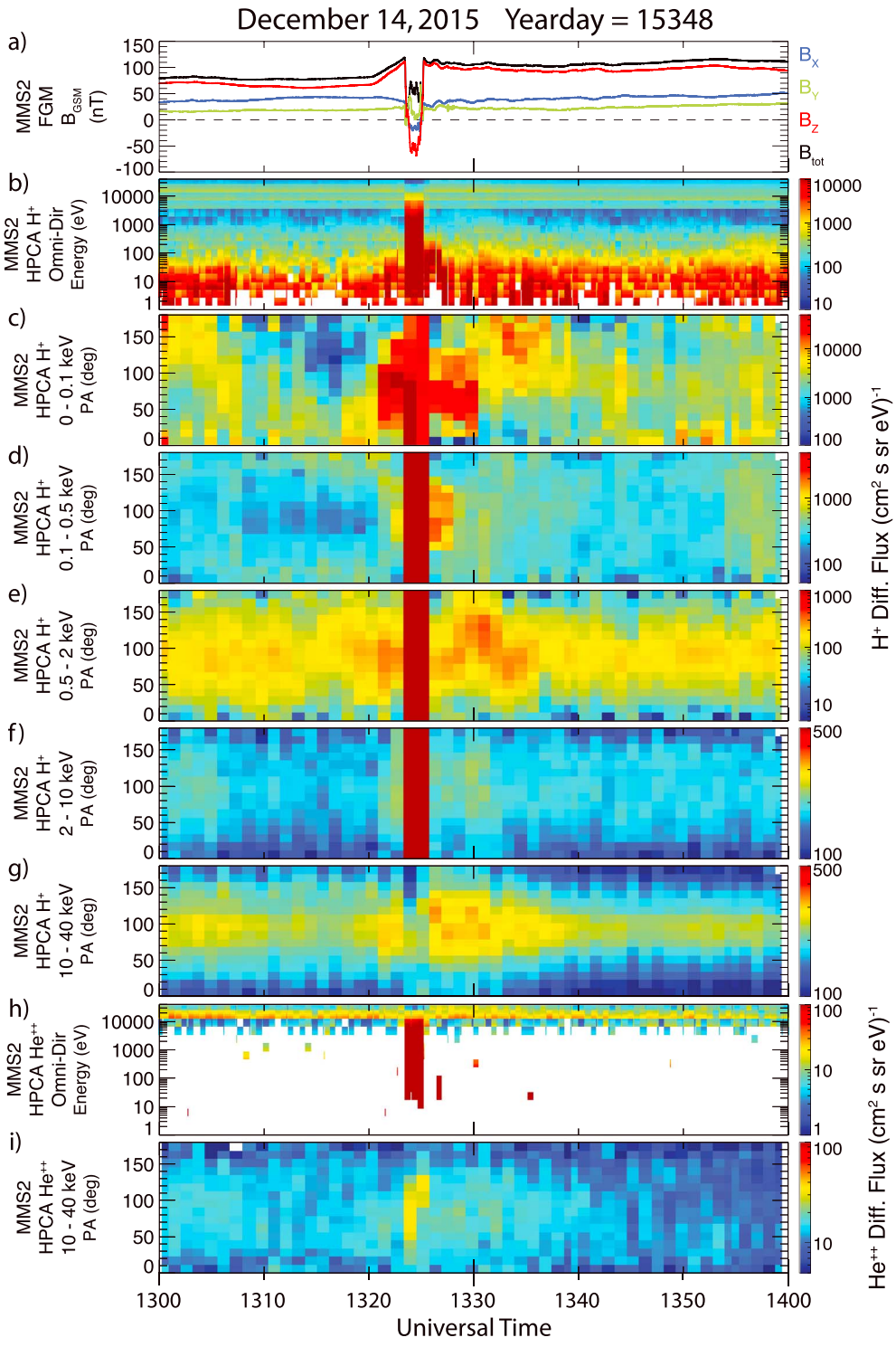

Figure 11. MMS 2 magnetic field and Hot Plasma Composition Analyzer (HPCA) observations from 1300 to 1400 UT on 14 December 2016. (a) A plot of the GSM components and total field (Bx, By, Bz, and Btot). (b) An energy spectrogram of the omnidirectional fluxes of protons. (c–g) Pitch angle spectrograms of protons with the indicated energy ranges, from low to high. (h) An energy spectrogram of the omnidirectional fluxes of He^{++} ions. (i) A pitch angle spectrogram of He^{++} ions with energies from 10 to 40 keV.

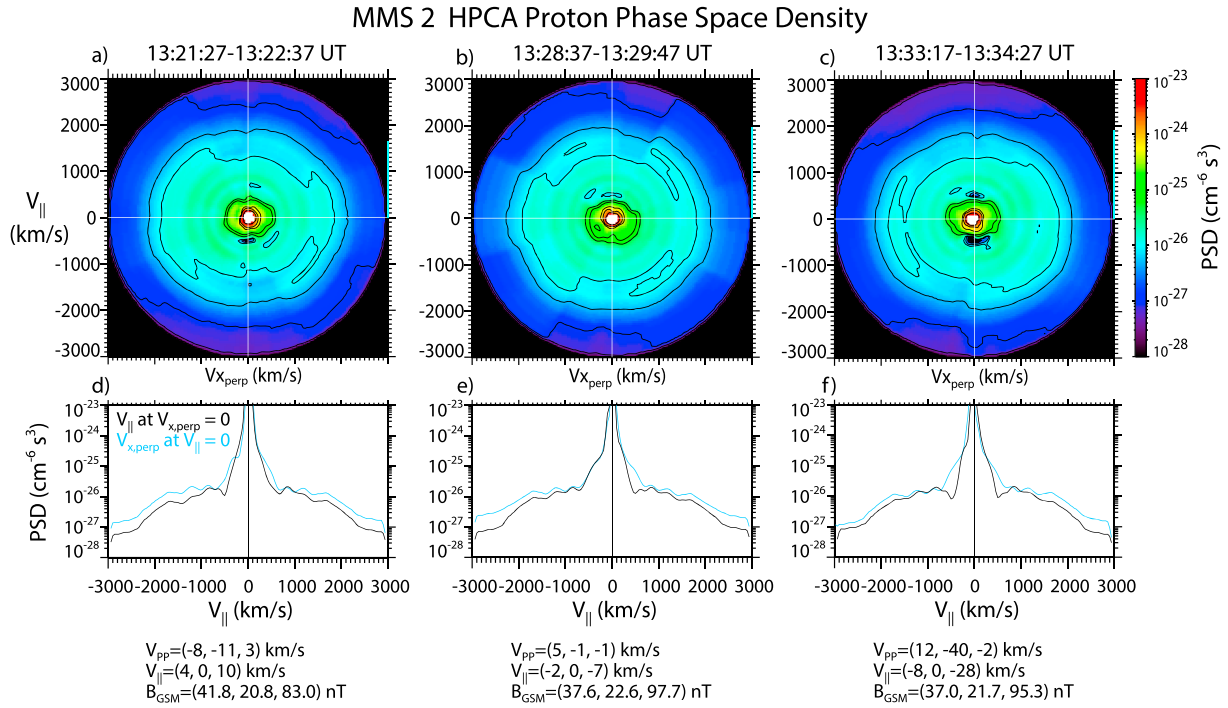

Figure 12. Proton phase space density distributions measured by the MMS 2 Hot Plasma Composition Analyzer (HPCA) instrument before the magnetosheath intrusion (13:21:27–13:22:37 UT), 2 min after the retreat of the magnetosheath, and during the most intense electromagnetic ion cyclotron wave activity (13:28-37-13:29:47 UT), and ~5 min later, from 13:33:17 to 13:34:27 UT. (a–c) Color-coded 2-D distributions as a function of velocity parallel to the magnetic field (vertical axis) and perpendicular to it (horizontal axis). (d–f) 1-D traces of the phase space density in these two directions.

similar features to the protons at >10 keV/e, that population is a real signature of He^{++} that has persisted at low levels in the magnetosphere, rather than being an effect of proton contamination.

Figure 12 shows proton phase space density distributions measured by the MMS 2 HPCA instrument before the magnetosheath intrusion (13:21:27–13:22:37 UT), during the most intense EMIC wave activity 2 min after the retreat of the magnetosheath (13:28-37-13:29:47 UT), and ~5 min later, from 13:33:17 to 13:34:27 UT. Figures 12a–12c show 2-D distributions color-coded according to the color bar at the right. The vertical axis $V_{||}$ in each panel is parallel to the local magnetic field, **B**, and the horizontal axis Vx_{perp} is perpendicular in the direction of **(B** × **u)** × **B**, where **u** is the proton bulk velocity unit vector. Distributions with horizontal axis Vy_{perp} in the **B** × **u** direction (not shown) were very similar in each time interval. Figures 12d–12f show 1-D traces of the phase space density in the $V_{||}$ and Vx_{perp} directions, averaged over 10 velocity bins on each side of the center bin, hence over a range of ±400 km/s. In the velocity range beyond 1,000 km/s, the phase space density values were more than a factor of 30 above the 1-count level. Both the 2-D and 1-D distributions show modest temperature anisotropies over much of the velocity range during all three time intervals, as well as evidence of ring-like distributions with relatively weak gradients. The ring structure is most clearly shown in Figure 12e, immediately after the retreat of the magnetosheath: the phase space densities in both traces appear to rise and fall together in three peaks between 800 and 1,600 km/s.

Figure 13 presents particle data and the Blum et al. (2009) EMIC instability proxy for the interval between 1300 and 1400 UT. Figure 13a shows the total plasma density, calculated using two different values of the total number density of the plasma. Because the Fast Plasma Instrument (FPI) on the MMS spacecraft was not operating during the 1300–1400 UT interval, and the upper hybrid and plasma frequency lines were not sampled, we rely on two alternate methods. The total ion density in the 1 eV–40 keV energy range measured by the HPCA instrument provides a lower bound (grey line). The black line is calculated using the total electron number density determined by a model fit of the spacecraft potential following the procedures outlined in Andriopoulou et al. (2018). This more sophisticated method of calculating total density provides a value that still has uncertainties that could result in it being either higher or lower than the true value. Instabilities calculated using both densities are of value, as noted in a discussion of total density proxies in

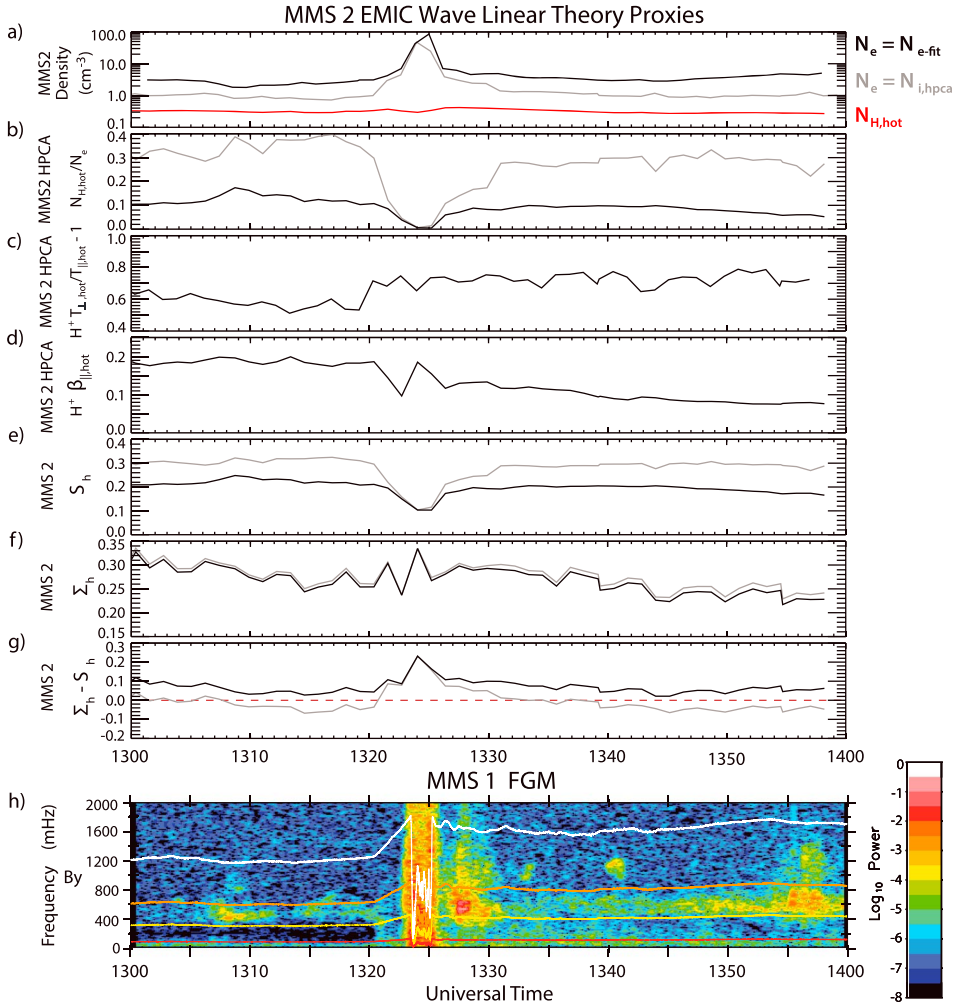

Figure 13. Electromagnetic ion cyclotron linear theory proxies calculated from MMS 2 data. (a) Total plasma densities determined using the spacecraft potential (black line) and the total ion density measured by HPCA (grey line), and hot plasma density (red line). (b) Ratios of hot proton density to total plasma density, calculated using total plasma densities determined from the spacecraft potential (black) and the total ion density measured by HPCA (grey). (c) Anisotropy of hot protons (10–40 keV) measured by the HPCA instrument on MMS 2. (d) Plasma beta of hot ions parallel to the magnetic field. (e) Theoretical Blum et al. (2009) instability threshold parameter S_h calculated using both total plasma density values. (f) Experimental Blum et al. (2009) instability parameter Σ_h. (g) Σ_h-S_h, calculated using both S_h values. (h) Fourier spectrogram of the By (azimuthal) component of differenced magnetic field data in local field-aligned coordinates from MMS 1 from 1300 to 1400 UT on 14 December 2015, as in Figure 5b.

Cluster data in Appendix A of Allen et al. (2016). The density of the hot protons is also shown in Figure 13a (red line).

Figure 13b shows the ratios of hot proton density to total plasma density, calculated using each of the above total density values. Figures 13c and 13d present the anisotropy of hot protons (10 keV–40 keV) and the parallel plasma beta for these hot protons, respectively, based on data from the HPCA instrument on MMS 2. Figure 13e shows the theoretical instability threshold parameter S_h. Figure 13f shows the experimental instability parameter Σ_h, and Figure 13g shows the instability proxy, Σ_h-S_h. Following Blum et al. (2009), when this difference is positive, the plasma is predicted to be unstable to EMIC growth. Figure 13h repeats Figure 5b in showing a Fourier spectrogram of the magnetic field data during this interval.

The two total density values shown in Figure 13a are in good agreement during the brief magnetosheath encounter, but the factor of 2–4 difference at other times in the 1300–1400 UT interval reflects the higher density recorded using the spacecraft potential than that measured by HPCA. Because the density of hot

ions was nearly constant, Figure 13b shows that the resulting ratio of hot to total ion density depends (inversely) primarily on the total density value. Figure 13c shows that the temperature anisotropy was near 0.6 before 1320 UT and rose to near 0.75 afterward, with only minor variations either before or after the magnetospheric compression. This is consistent with the distributions shown in Figure 12. The parallel hot ion beta (Figure 13d) was relatively constant near 0.18 before 1320 UT but fell off gradually from 0.13 at 1326 UT to 0.08 at 1357 UT. The difference in the two curves shown in Figure 13e again reflects the higher density derived from the spacecraft potential than that measured by HPCA: higher total plasma density lowers the instability threshold. Figure 13f shows that Σ_h was largest from 1300 to 1310 UT and from 1325 to 1340 UT and fell off slightly after that time.

Comparison of the instability proxies (Figure 13g) and the wave spectrogram indicates that both proxies were highest during the magnetosheath incursion and during the few minutes afterward (1326–1330) when the largest amplitude EMIC waves were observed, consistent with increased levels of cold plasma. The positive values of both proxies indicate that the instability criterion is met for MMS to be passing through a source region, so this may explain why multiple wave packets were observed in Figures 7–10. The proxy using HPCA ion densities (grey line) was negative or zero at all other times, but the proxy using densities derived from the spacecraft potential (black line) remained positive during the entire 1300–1400 UT interval, qualitatively consistent with the occurrence of EMIC waves both before and after the compression. We note also the rather small range of temporal variations in both the grey and black lines before 1320 and after 1330 UT, during times EMIC waves were observed as well as when they were not observed. As we will note below, this is consistent with other studies that have inferred that EMIC waves can act promptly to bring the plasma below an *instability threshold*.

3.3. Van Allen Probes Observations

The compression stimulated a complex H band EMIC wave burst at Van Allen Probe A (L = 5.65, MLT = 12.8 hr, MLAT = 3.2°), as shown in Figure 14, but no EMIC waves were observed by Van Allen Probe B. Figure 14a shows the spin-averaged differential proton flux recorded by the HOPE instrument on Van Allen Probe A from 1300 to 1400 UT. An energetic ring current population above 10 keV and a lower energy population (below ~1 keV) both appeared throughout this interval. The energy of both populations increased from 1320 UT to near 1325 UT, approximately following the increase in the magnitude of the magnetic field, and slowly decreased in energy from 1325 to 1400 UT (Figures 14b and 14e).

EMIC waves began near 1324:30 UT (Figure 14b), near the time these ions reached their maximum energy. A ~1.0 Hz emission with mixed but mostly linear polarization and maximum amplitude of 2.9 nT rms near 1327 UT continued with diminishing amplitude until 1336 UT. A rising-frequency 0.7 nT rms amplitude triggered emission (Omura et al., 2010; Pickett et al., 2010) appeared in both Bx (not shown) and By with purely left-hand polarization (Figure 14c) at 1326:10 UT, with frequency rising from 1.0 to 2.0 Hz in ~20 s. Between 1327 and 1329 a weak 1.6–2.0 Hz emission also appeared with slightly rising frequency, mixed polarization, and gradually decreasing amplitude. All of these waves had wave normal angles near 0° (Figure 14d).

Figures 15a–15c show 2-D distributions of the HOPE proton flux at three representative times during this interval. The three plots are very similar in showing temperature anisotropies at and above 5 keV, from ~200 to 1,000 eV, and below 100 eV, and a ring-like distribution at and above 5 keV with a relative minimum in fluxes below it. The perpendicular fluxes and energies of the ions in the two upper energy ranges were higher during the time strong EMIC waves were observed (Figure 15b) than at the earlier or later times. Both the increased temperature anisotropy and the ring distribution can lead to EMIC wave generation (Lee & Angelopoulos, 2014).

Instability proxies were also calculated for Van Allen Probes A and B data. As was the case for MMS, a direct measurement of the total ion density was not available for Van Allen Probes A during this interval. The HOPE instrument on Van Allen Probes A does not measure ions at the lowest energies, but the HOPE electron density provides useful information during this event. The spacecraft is positively charged relative to the ambient plasma when outside the plasmasphere due to photoemission. This means that the spacecraft body expels ions but attracts electrons. Consequently, the HOPE electron density provides a better estimate of the density than the ions when the spacecraft is positively charged.

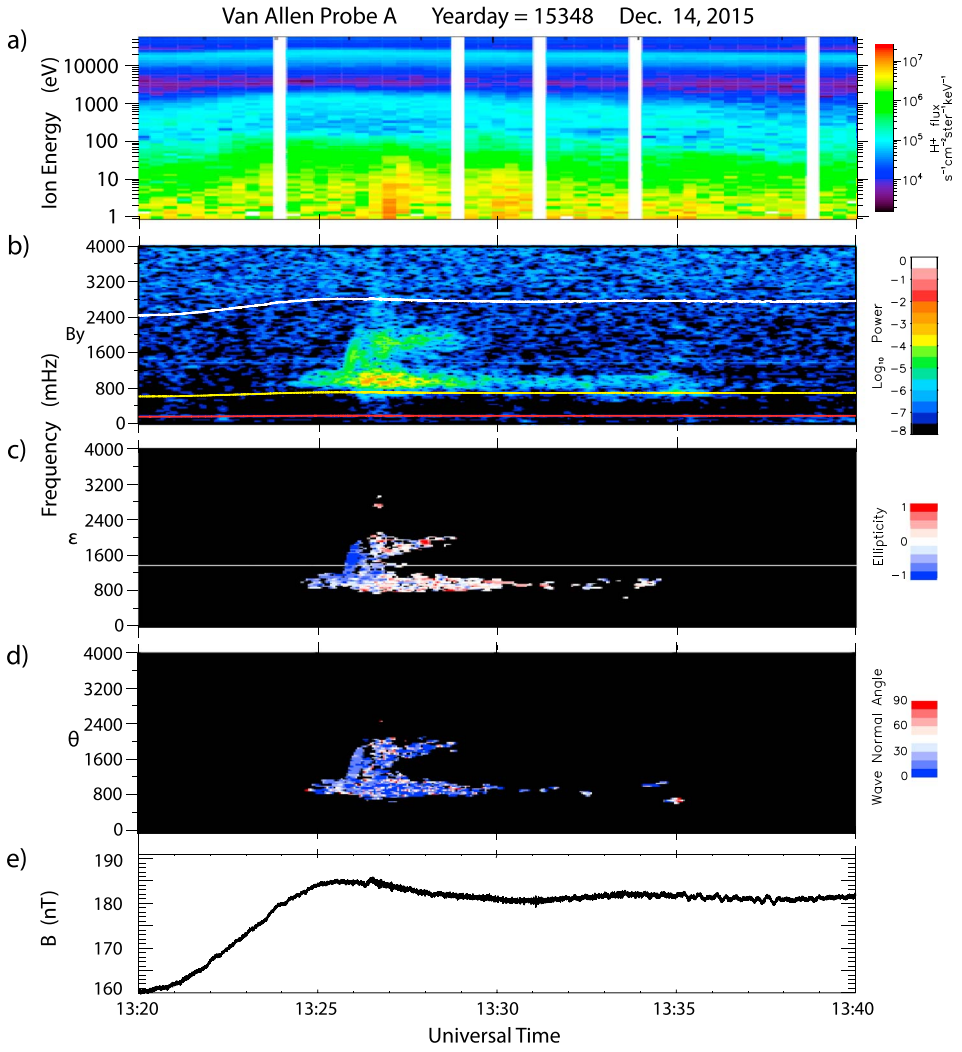

Figure 14. Van Allen Probe A HOPE energetic proton and EMFISIS magnetic field data from 1320 to 1340 UT on 14 December 2015. (a) Energy versus time spectrogram of the spin-averaged differential proton flux. (b) Frequency versus time spectrogram of By (azimuthal) component magnetic field data in local field-aligned coordinates. (c) Wave ellipticity. (d) Wave normal angle. (e) Total magnetic field. The white line in panel c is a harmonic of the satellite spin frequency.

Thus, as in Figure 13, we show in Figure 16a three traces: the grey line shows the total H^+ density measured by HOPE, the black line shows the total HOPE electron density, and the red line shows the *hot* (3 to 30 keV) H^+ density. The other panels of Figure 16 show quantities corresponding to those in Figure 13. As was the case for MMS, during the time strong EMIC waves were observed, from 1325 to 1330 UT, Figure 16b shows that the ratio of hot protons to total protons (grey) and to electrons (black) measured by the HOPE instrument on Probe A fell, and Figure 16c shows that the hot proton anisotropy increased slightly. The black line in Figure 16g showing the instability proxy $\Sigma_h - S_h$ neared or exceeded 0 only between 1325 and 1330 UT, but the grey line never exceeded −0.08. A later relative maximum near 1350 UT in both traces occurred near the beginning of relatively weak 600 mHz EMIC wave activity. The difference $\Sigma_h - S_h$ calculated for Probe B between 1300 and 1400 UT (not shown) never rose above −0.16 using either density value, indicating no instability, consistent with the absence of EMIC waves at that spacecraft.

3.4. GOES 13 Observations

The compression-initiated EMIC wave burst observed at GOES is shown in Figure 17. Panel a is a Fourier spectrogram of differenced radial (He) component data in the GOES Hp, He, and Hn coordinate system (Hp

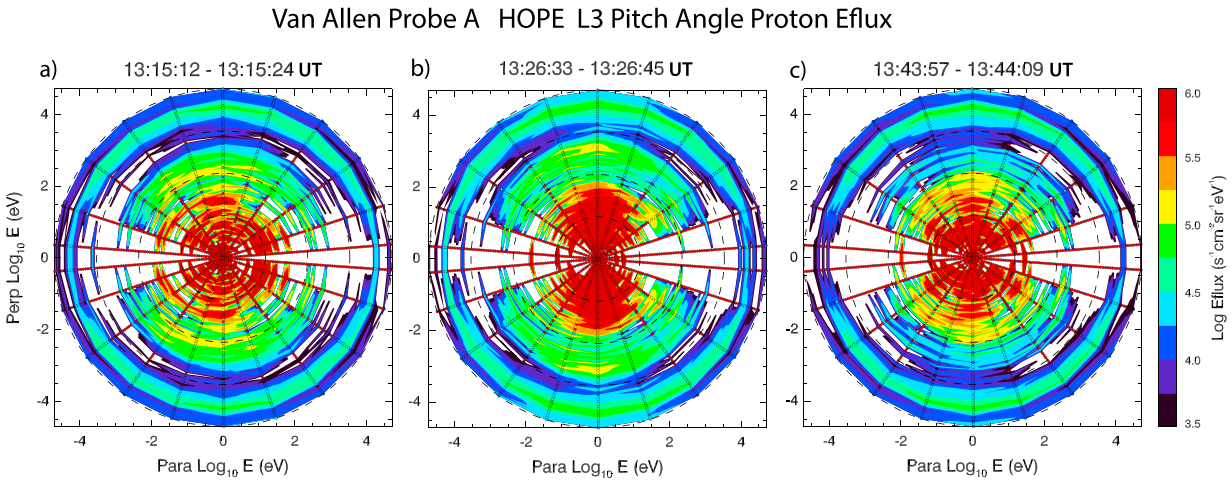

Figure 15. Proton data from the HOPE instrument on Van Allen Probe A on 14 December 2015. (a–c) Two-dimensional distributions of the proton flux at 1315 UT, before the magnetospheric compression (panel a); at 1326 UT, near the time of the peak compression of the magnetic field and during the electromagnetic ion cyclotron wave event (panel b); and at 1343 UT, after the compression (panel c).

positive northward parallel to Earth's rotation axis, He in the Earthward direction, perpendicular to Hp, and Hn in the Eastward direction, perpendicular to Hp and He). Panel b shows the ellipticity associated with this burst, calculated using the He and Hn (azimuthal) components. Panel c shows the magnitude of B. The wave burst began simultaneously with the increase in the total magnetic field near 1323 UT, reached its peak amplitude of ~0.4 nT near 1325 UT, 1 min before the time of maximum B, and diminished in amplitude as B decreased after 1327 UT. Detailed line plots between 1325 and 1327 UT (not shown) indicated that after 1326 UT wave packets appeared independently in the two transverse components, consistent with the predominantly linear polarization shown in panel b.

4. Propagation and Timing of the Initial Wave Burst

The estimated time of the shock impact on the magnetopause based on OMNI data was 1318 UT (Cattell et al., 2017). Figure 1 of Cattell et al. (2017) shows the temporal progression of the magnetospheric compression from MMS 1 to Van Allen Probe A and GOES 13. The compression was first observed near 1320:15 UT at MMS 1 (L = 9.7, MLT = 13.0 hr), near 1321 UT at Van Allen Probe A (L = 5.7, MLT = 12.9 hr), and near 1323 UT at GOES 13 (L = 6.8, MLT = 8.7 hr). The successive time delays between compression onsets at MMS 1, Van Allen Probe A, and GOES 13 were thus ~1 and ~3 min. The incursion of the magnetosheath inside the orbit of MMS 1 allows us only to set bounds on the time of the peak dayside compression at that location, between 1323:27 and 1325:15 UT (Figure 3a). The magnetic field at Van Allen Probe A peaked at 1325:32, but with a second, short-lived peak at 1326:32 (Figure 14d), and the field at GOES 13 peaked at 1326:55 UT (Figure 17c). Based on their analysis of data from ARTEMIS, Wind, and ACE, Cattell et al. (2017) found that the shock was inclined and would likely have impacted the dawnside of the magnetosphere first. Because both the first impact of the compression and the peak compression-induced magnetic field at GOES 13 occurred later than that at Van Allen Probe A, however, we infer that the shock impacted the magnetosphere at only a slightly prenoon local time.

EMIC wave bursts, however, did not occur immediately after the beginning of the increase in B at MMS or Van Allen Probe A. The wave onset at MMS was delayed until 1326 UT, by which time the magnetopause had retreated sunward, and wave onset at Van Allen Probe A began at 1324:30 UT, ~4 min after the initial rise in B. Only at GOES 13 did waves begin roughly simultaneously with the initial rise in B.

Figure 18a shows differenced magnetic field spectrograms of azimuthal component data from MMS 1, and Figures 18b–18e show differenced north-south component data from the four ground stations shown in Figure 2. Presentation of different components for satellite and ground data reflects the theoretically predicted 90° rotation of the plane of polarization of transverse ULF waves from the magnetosphere to the ground, caused by the lack of penetration of field-aligned currents into the atmosphere (Hughes, 1974;

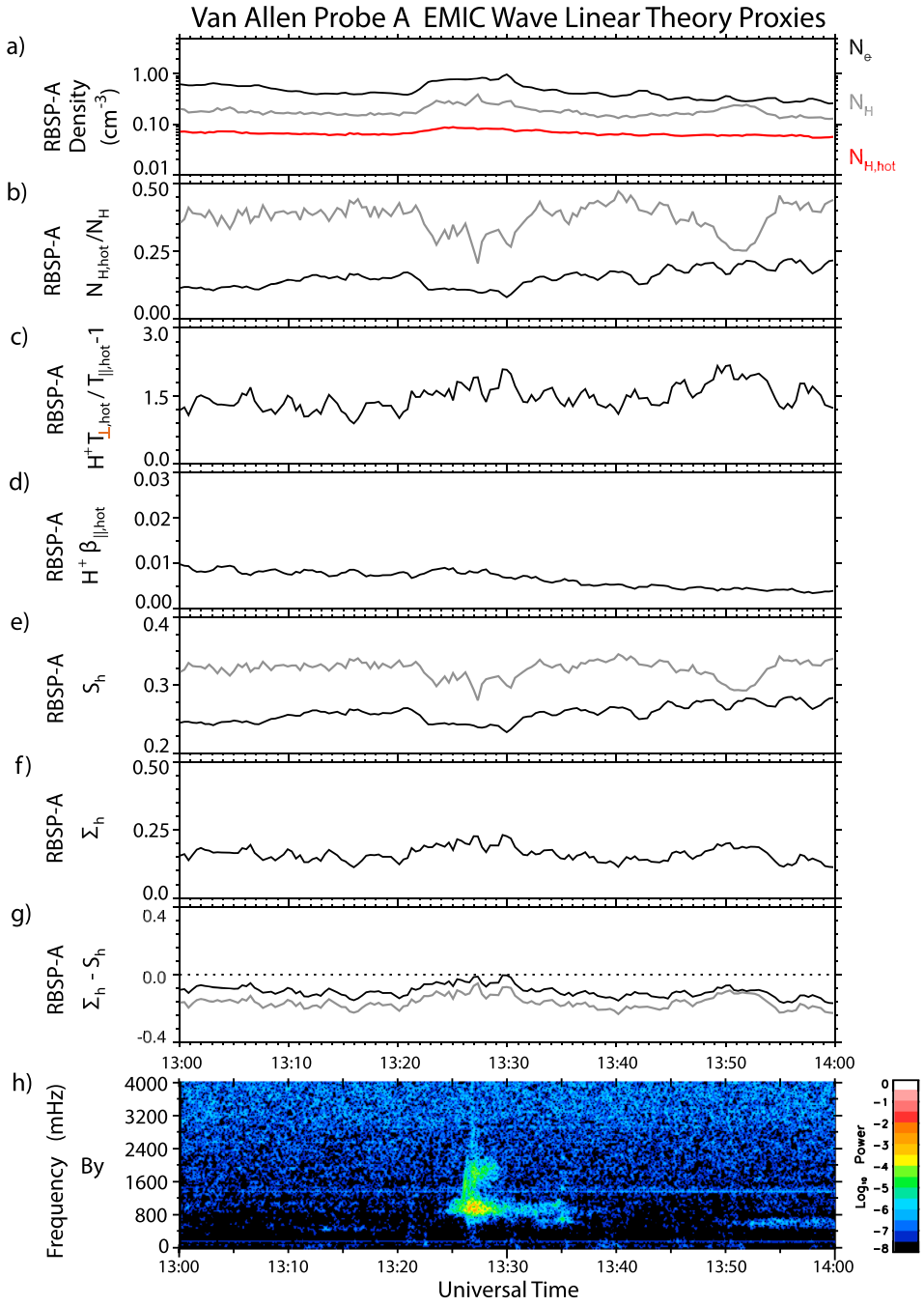

Figure 16. Electromagnetic ion cyclotron linear theory proxies calculated from Van Allen Probes A (RBSP-A) data. (a) Total plasma densities determined using the HOPE electron density (black line) and HOPE proton density (grey line), and hot plasma density (3 to 30 keV; red line). (b) Ratios of hot proton density to total proton densities measured by HOPE (electrons, black line, and protons, grey line). (c) Anisotropy of 10 eV–30 keV protons measured by HOPE. (d) Plasma beta of 10 eV–30 keV protons parallel to the magnetic field. (e) Theoretical Blum et al. (2009) instability threshold parameter S_h. (f) Experimental Blum et al. (2009) instability parameter Σ_h. (g) Σ_h-S_h. (h) Fourier spectrogram of the By (azimuthal) component of differenced Van Allen Probes magnetic field data in local field-aligned coordinates from 1300 to 1400 UT on 14 December 2015, as in Figure 4b.

Hughes & Southwood, 1976). For Pc3–5 waves this rotation is easily visible, because the wave structure is strongly asymmetric (the latitudinal scale is much smaller than the longitudinal scale). This polarization rotation was also predicted theoretically by Greifinger (1972a, 1972b) for Pc 1 waves. However, for Pc1–2

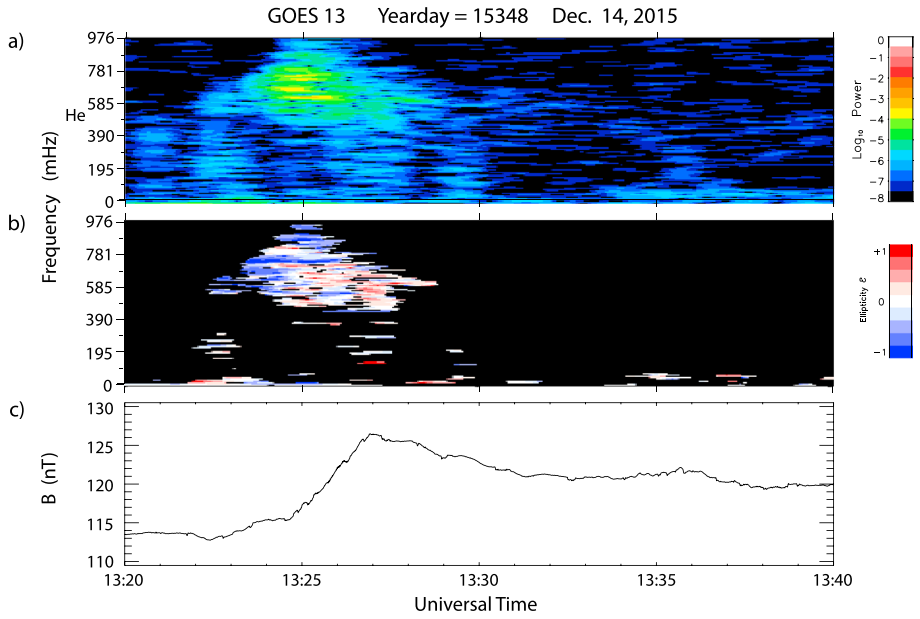

Figure 17. GOES 13 magnetic field data from 1320 to 1340 UT on 14 December 2015. (a) Frequency versus time spectrogram of He (earthward) component magnetic field data. (b) Wave ellipticity. (c) Total magnetic field.

waves such an asymmetry is often not pronounced (the waves are often elliptically or even circularly polarized), and the rotation effect is difficult to identify.

Figures 18b and 18c show wave power in search coil data from AAL-PIP PG3, Antarctica, and Sondrestromfjord, Greenland. These stations are located at nearly the same magnetic local time (10.8 and 10.9 hr MLT, respectively), slightly over 2 hr MLT earlier than (west of) the footpoint of MMS 1 but at nominal L values of 10.6 and 13.0, respectively, ~1 and ~2.5 L higher than MMS 1. Figures 18d and 18e show wave power in search coil data from South Pole Station, Antarctica, and fluxgate data from Pangnirtung, Canada, respectively. These stations are located ~1 hr farther west in local time (9.8 and 9.7 hr MLT, respectively), and at nominal L values of 12.4 and 14.1, ~3 and ~4.5 L higher than MMS 1. Six other magnetometers in the MACCS, MICA, and AAL-PIP arrays also observed EMIC waves at the time of this compression (not shown), at local times extending dawnward to 8.3 hr MLT. The MICA magnetometer at Hornsund, Svalbard, (L = 13.7, 16.3 hr MLT), however, saw no EMIC activity at this time.

EMIC waves associated with the compression and with frequency between 0.3 and 0.8 Hz appeared beginning near 1321 UT at AAL-PIP PG3, Sondrestromfjord, and South Pole Station and beginning near 1324 UT at Pangnirtung; they ended near 1329 UT at all four stations. The strong transverse 0.3–0.8 Hz EMIC wave burst at all four MMS spacecraft, however, did not begin until 1326 UT, after an ~1-min interval of quiet magnetic fields following the outward retreat of the magnetopause, and ended near 1330 UT, 1 min later than on the ground.

Other wave activity shown in Figure 18, from 1315 to 1320 UT, 1345 to 1349, and 1356 to 1400, appeared at three or four ground stations but did not occur at the same times or with the same frequencies as waves observed by MMS 1.

5. Discussion

A complex set of EMIC waves was observed at several locations in the outer dayside magnetosphere before, during, and after the modest magnetospheric compression that occurred on 14 December 2015. Yahnin et al. (2015) noted that in many cases when solar wind compressions stimulated EMIC waves, weak wave activity was evident in the outer dayside magnetosphere even before compression onset. They interpreted this to mean that this region was near marginal instability to EMIC wave generation before the compression. Their conclusion applies to this event as well, and it is also consistent with the instability proxy at MMS 1

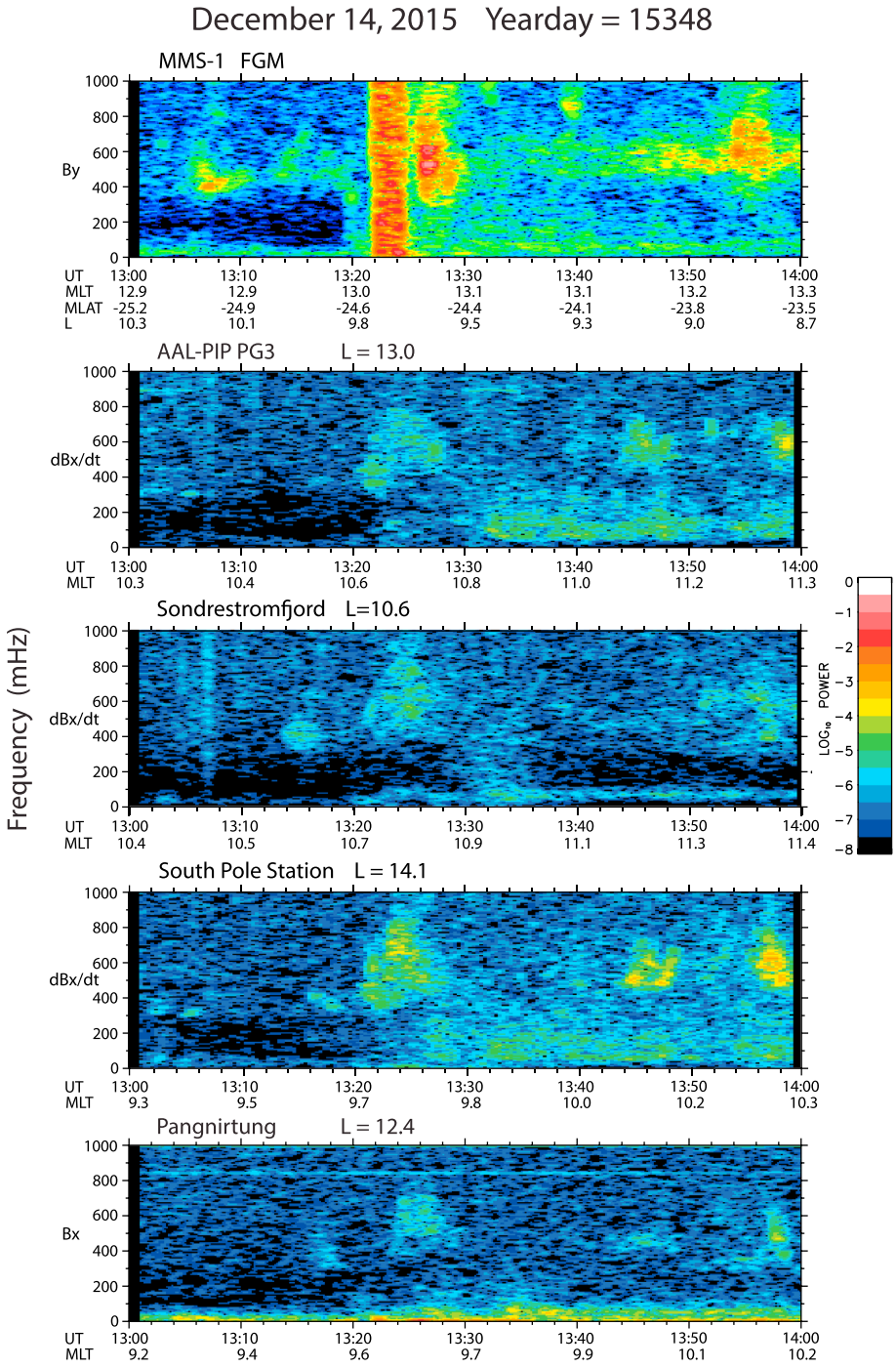

Figure 18. Spectrograms of differenced magnetic field data from MMS 1 and four high-latitude ground stations between 1300 and 1400 UT on 14 December 2015, grouped in order of decreasing local time.

(Figure 13). Because no ion data at ring current energies were measured by GOES 13, we cannot provide a quantitative explanation for the differences in the timing of wave onset relative to compression onset between Van Allen Probe A and GOES 13, namely, that although the compression onset was observed later at GOES 13 than at Van Allen Probe A, EMIC wave onset began earlier. We can only speculate that because GOES 13, situated at larger L than Van Allen Probe A and on the dawn side, was immersed in a plasma that was nearer the point of instability to EMIC waves, only a modest compression was needed to trigger wave onset.

The continuation of EMIC wave activity for up to 2 hr after the initial compression is also consistent with earlier observations by Usanova et al. (2010), using data from CARISMA and STEP ground magnetometer arrays and the Cluster satellites; the generation of the EMIC waves and consequent loss of energetic protons may last for several hours while the magnetosphere remains compressed.

Our observations at both MMS and Van Allen Probes A have confirmed that the Blum et al. (2009) instability proxy Σ_h-S_h was increased during the few-minute interval after 1325 UT when EMIC waves were observed. At MMS a modest increase in hot proton temperature anisotropy was counterbalanced by a decrease in parallel proton beta, while at Van Allen Probe A both the hot proton temperature anisotropy and parallel proton beta showed modest increases.

Several observational studies since 2009 have also evaluated EMIC instability criteria. Spasojevic et al. (2011) found a good correspondence between predictions from the Blum et al. (2009) inverse relation and subauroral proton precipitation, which is now understood to result from interactions with EMIC waves. Statistical studies by Lin et al. (2014), using Cluster data, and Noh et al. (2018), who used Van Allen Probe A data, evaluated both the Kennel and Petschek (1966) hot proton anisotropy and the Blum et al. (2009) instability proxy, which includes both the hot proton anisotropy and the hot parallel ion beta.

Lin et al. (2014) concluded that the proton anisotropy is necessary but not sufficient alone for excitations of ion cyclotron waves and noted limitations of predicting the instability using the Blum et al. (2009) inverse relation. Noh et al. (2018) used the proton anisotropy determined using the proton distribution measured over a wide ring current energy range and found a significant overlap in the anisotropy ranges between times with and without EMIC waves, but that there was a small increase in the Kennel-Petschek anisotropy in a statistical sense from just prior to EMIC wave onsets to just after EMIC onsets. Noh et al. (2018) also found a significant overlap between the values of Σ_h-S_h during times with and without EMIC waves, and a statistical increase in Σ_h-S_h from ~60% unstable (>0) during non-EMIC times to over 75% during EMIC events. They also noted that their results imply that the proton distributions must often stay close to a marginal state, with anisotropies close to threshold values for ion cyclotron instability, as noted also earlier by Gary et al. (1994). This is consistent with the remarkably similar values of Σ_h-S_h shown in Figure 13g during times EMIC waves were or were not observed in the outer magnetosphere.

The availability of ground-based observations at very high latitudes approximately 2 and 3 hr MLT west of the footpoint of the four MMS spacecraft makes it possible to infer the excitation of EMIC waves in the outer regions of the dayside magnetosphere even before the magnetosheath penetrated inward of the orbit of the four MMS spacecraft. As the shock-induced compression first propagated inward from the magnetopause beginning at 1318 UT (the time inferred from OMNI data), it stimulated EMIC waves on the outermost marginally stable dayside L shells near or slightly south of the magnetic equator and somewhat dawnward of noon. These waves then propagated both northward and southward along magnetic field lines at the local Alfvén speed until they reached the ionosphere. An estimate of this wave traveltime was prepared following the assumptions in the Appendix of Chi and Russell (1998). Assuming an equatorial number density of 1/cm^3 at L = 12–14, somewhat lower than the MMS observation of 2–4/cm^3 at L = 10, this gives a traveltime range from 1.9 to 3.6 min. Using a traveltime of 2–3 min gives a wave onset time at the ground stations of 1320–1321 UT, consistent with observations.

As Cattell et al. (2017) noted, the compression also continued to propagate radially inward and earthward, but it did not do so at the fast mode speed (~1000 km) but at a much lower speed that may have been related to the speed of the inward motion of the magnetopause (ranging from ~50 km/s to a few 100 km/s), thus taking 2–3 min to reach the MMS spacecraft, located 3–5 R_E inward from the precompression magnetopause and ~ 1 hr MLT duskward of noon. As a result, the first appearance of the 0.3–0.8 Hz EMIC wave burst at three of the four ground stations and the initial rise of the magnetic field at MMS-1 both occurred between 1320 and 1321 UT.

We noted above the nearly identical frequency range of the wave bursts observed on the ground and at MMS before 1330 UT. Could they originate in the same source or at least on the same L shell? The latter is reasonable, because after the retreat of the magnetopause, flux tubes near the magnetospheric boundary moved outward past the spacecraft.

The timing of the wave observations on the ground and at MMS, however, is inconsistent with their having the same source location. If the waves observed by MMS were generated near the equator, one would expect that they would propagate earthward and might appear 2–3 min later on the ground. The wave packet observed on the ground, however, ended 1 min earlier than the wave packets at MMS. This suggests that the wave packet observed at MMS, located 2–3 hr MLT later than the ground stations, was not ducted longitudinally to the ground stations.

One might also consider that if the wave generation regions were significantly far from the magnetic equator, consistent with daytime distortion of outer magnetospheric field lines (e.g., Allen et al., 2013, 2015, 2016; Liu et al., 2012, 2013), especially in association with a brief compression, then it is possible that waves from the same source might reach MMS and the ionosphere at roughly the same time, as observed. (Although the distance from the generation region to the ionosphere may be much larger than the distance to the equator, the wave speed increases greatly as the field line nears Earth.) However, the near simultaneity of the waves at high-latitude ground stations in both hemispheres makes it unlikely that these waves were generated asymmetrically in latitude far from the equator.

We have noted that beginning at 1326 UT, each MMS spacecraft encountered intense electromagnetic waves with linearly polarized ~1.75-s period waves that appeared to be relatively independent in the radial Bx component and the azimuthal By component. What factors might cause the azimuthally and radially polarized waves to appear together, but with different temporal wave packet structures and amplitudes, and with slightly different frequencies?

First, it is possible that in some way waves with these different polarizations and amplitudes, and with slightly different frequencies, could have been generated on the L shell at which the MMS spacecraft were located at this time and guided along the same path to the location of MMS. Because the EMIC wave proxy results suggest that the region near MMS was suitable for wave generation, MMS may have been within the source region even though it was located ~25° south of the magnetic equator. Allen et al. (2015) observed many EMIC waves in the outer dayside magnetosphere with Cluster, and Allen et al. (2016) showed that many of them were locally generated off-equator, possibly in association with Shabansky orbits (McCollough et al., 2010, 2012). Because the compression may have created a large latitudinal region of unstable plasma with slightly different plasma distributions, it is conceivable that waves with different polarizations (and even slightly different frequencies) could have been generated at different latitudes.

It is also possible that these waves might have been generated at higher L shells (either at the equator or at off-equatorial locations) and subsequently refracted inward as they propagated away from their source and then reflected at intermediate latitudes (e.g., Kim & Johnson, 2016) to return toward and across the equator. If their refraction was polarization-dependent, a consequence of plasma birefringence (e.g., Segre, 1994), this could even explain why the radial and azimuthal components were largely independent. Waves with different polarizations might be generated together at a given L shell, but the radially polarized waves might have been refracted more than the azimuthal waves, so that waves with different frequencies (generated at slightly different L shells) could appear at the location of MMS.

A third possibility, consistent with generation on the L shell at which the MMS spacecraft were located, involves mode conversion from magnetosonic waves at near-equatorial ion-ion hybrid resonance locations in an inhomogeneous plasma (Kim et al., 2008, 2013, 2015; Lee et al., 2008). If the plasma density gradient is in the radial direction, the resulting transverse waves are predicted to be linearly polarized in the azimuthal meridian and have field-aligned Poynting flux (Kim et al., 2008), consistent with our observations. However, these theoretical studies did not specify how linearly polarized waves might also be excited in the radial meridian or make any predictions about the wave normal angle, which in the case observed here was near 0°.

In addition to the commonly observed minimum in transverse EMIC wave power near the equatorial He^{+} gyrofrequency, the interval from 1300 to 1400 UT was unusual in the presence of a similar minimum at the He^{++} gyrofrequency, which can be associated with the presence of He^{++} ions. This has been observed before within the magnetosheath (Anderson et al., 1994; Denton et al., 1993, 1994) and is consistent with a solar wind origin for these ions, but a recent study by Yu et al. (2017), also based on MMS data, is to our knowledge the only other report of such a minimum within the magnetosphere. The observations reported here, along with those of Yu et al. (2017), indicate that at least under some conditions He^{++} ions can affect the wave

Table 2
Mean Correlations and Their Standard Deviations Between Corresponding Waveforms at the Four MMS Spacecraft During the Time Intervals Shown in Figures 8 and 10

Interval:	13:27:15–13:28:15 UT			13:40:00–13:41:00 UT		
Component:	*X*	*Y*	*Z*	*X*	*Y*	*Z*
Spacecraft Pair						
1–2	0.968	0.984	0.989	0.983	0.993	0.962
1–3	0.930	0.945	0.890	0.778	0.813	0.801
1–4	0.983	0.990	0.979	0.950	0.960	0.929
2–3	0.892	0.909	0.866	0.728	0.778	0.770
2–4	0.950	0.964	0.963	0.927	0.944	0.914
3–4	0.980	0.981	0.955	0.920	0.933	0.905
Mean:	0.951	0.962	0.940	0.881	0.904	0.880
	±0.034	±0.031	±0.051	±0.103	±0.087	±0.076

populations in the outer magnetosphere. We note also that the two left-hand circularly polarized 1 Hz wave bursts observed near 1332 and 1340 UT both occurred at frequencies above the He^{++} gyrofrequency. Anderson et al. (1994) often observed left-hand polarized EMIC waves above the He^{++} gyrofrequency in the magnetosheath, and this polarization is consistent with the theoretical H^{+}-He^{++} plasma wave dispersion modeling of Denton et al. (1993).

As part of a study of a transient dayside subauroral precipitation event, Fuselier et al. (2004) reviewed the physical mechanism for solar wind shock-induced generation of EMIC waves. They noted that the location(s) of wave growth would depend critically on how and where the growth rate of the EMIC instability increases in the equatorial outer magnetosphere and pointed out that in an adiabatic compression the temperature anisotropy, hot and cold plasma densities, perpendicular temperature, and magnetic field can all increase. Analysis of MMS HPCA data between 1300 and 1400 UT suggests that several of the EMIC wave bursts that occurred were driven by increases in the proton temperature anisotropy, but the instability that stimulated the more intense EMIC waves that occurred shortly after the outward movement of the magnetopause was also driven by an increase in cold plasma density relative to its value before the compression.

Finally, we noted the strong similarities between the waveforms observed by the four MMS spacecraft. Table 2 shows the correlation coefficients between the corresponding *X*, *Y*, and *Z* components at each pair of MMS spacecraft. With the exception of pairs including MMS 3, all the correlations were above 0.9 for both intervals and correlations between MMS 2 and MMS 3 were the lowest. Interspacecraft separations increased only slightly from 1325 to 1340 UT. MMS 4 and MMS 3 were separated by the smallest distance (10.3 to 10.5 km), and MMS 2 and MMS 3 were separated by the largest distance (28.6 to 30.0 km, mostly in the radial direction). These high correlations suggest that the coherence scale of the wave packets was on the same order as, or larger than, ~20 km. This result should not be surprising; these separations were considerably less than the ~150 km gyroradius of 10 keV ions. A statistical study currently underway will examine these wave coherence scales for cases in which the MMS spacecraft separations range from less than to greater than the gyroradii of ring current ions; this will be presented in a subsequent paper.

6. Summary

Detailed analysis of EMIC waves observed in the outer dayside magnetosphere before, during, and after the shock-induced magnetospheric compression on 14 December 2015 shows six features consistent with current theory, as well as two unusual or unexpected features.

1. The occurrence of waves before the compression is consistent with earlier observations by Yahnin et al. (2015) and Allen et al. (2015, 2016), suggesting that the outer dayside was near marginal instability to EMIC wave generation before the compression.
2. Intense waves were stimulated during or immediately after the initial compression as it propagated deeper into the magnetosphere, beginning near 1321 UT at the ground stations, near 1323 UT at GOES 13, and near 1324 at Van Allen Probe A. Intense waves were stimulated at all four MMS spacecraft ~1 min after the magnetopause rebounded outward.
3. The occurrence of waves during the further more gradual compression, from 1330 to 1530 UT, is consistent with earlier observations by Usanova et al. (2010).
4. The proton distributions observed by the HPCA instrument on MMS between 1300 and 1400 UT were consistent with the inverse temperature anisotropy-beta parallel relation of Gary et al. (1994) and the instability criterion of Blum et al. (2009). The wave growth parameter (Σ_h) did not substantially change during this interval, because the increase in hot H^{+} temperature anisotropy was counterbalanced by a decrease in the parallel plasma beta. However, the wave instability threshold (S_h) decreased following the compression, because the increase in cold plasma density reduced the hot-to-cold proton density ratio.
5. The proton distributions observed by the HOPE instrument on Van Allen Probes A during this same time interval were also consistent with the instability criterion of Blum et al. (2009). The wave instability

threshold (S_h) decreased during the times waves were observed, but at this spacecraft the wave growth parameter showed a modest increase. The proxy values Σ_h-S_h during most of the remainder of the 1300–1400 UT interval were lower than those for MMS. This is consistent with the absence of any EMIC activity during these times, in contrast to the occurrence of EMIC activity during much of this interval at MMS.

6. The waveforms observed at all four MMS spacecraft were remarkably similar, both during the unusual interval of short, linearly polarized wave packets between 1327:15 and 1328:15 UT and the more commonly expected interval of strongly left-hand polarized waves with longer wave packets between 1340 and 1341 UT. The spacecraft separations during both events were much less than the gyroradius of the hot ring current ions associated with them.

Two more unusual features were also observed during this event.

7. The EMIC waves observed at MMS shortly after the compression (between 1326 and 1330 UT) were a superposition of temporally independent wave packets linearly polarized in the transverse azimuthal and radial directions (in a local field-aligned coordinate system). These characteristics suggest the possibility of multiple source regions generating waves that reached the location of MMS (almost 25° below the magnetic equator) or of mode conversion from compressional waves.
8. A relative minimum in wave power at the He^{++} gyrofrequency in most of the wave events observed by MMS between 1300 and 1430 has rarely been observed but is qualitatively consistent with the increased density of He^{++} ions observed in the outer magnetosphere by the MMS HPCA instrument during this time. We note also that the two 1 Hz wave bursts observed near 1332 and 1340 UT both occurred at frequencies above the He^{++} gyrofrequency and were left-hand polarized. Both the relative minimum in wave power at the He^{++} gyrofrequency and the polarization of waves at frequencies above it are consistent with similar waves observed in the magnetosheath.

Future studies will investigate in more detail the wave properties of EMIC waves at higher L shells with MMS, as well as further investigating the evolution of the wave properties as they propagate, through data-model comparisons and advantageous conjunctions.

Acknowledgments

We thank David Sibeck, Viacheslav Pilipenko, Michael Schulz, Xiangrong Fu, Eun-Hwa Kim, and John Wygant for helpful comments, and we thank Shane Coyle and Dan Weimer for providing corrected AAL-PIP SCM data. Research at Augsburg University was supported by NSF grants AGS-1651263 and PLR-1341493. M. R. L. acknowledges support from NSF grant PLR-1341677. M. B. M. acknowledges support from NSF grant AGS-1654044. M. D. H. acknowledges support from NSF grant PLR-1543364. The dedication and expertise of the MMS development and operations teams are greatly appreciated. MMS work at JHU/APL, UCLA, UNH, and SwRI was supported by NASA contract no. NNG04EB99C. The work at New Jersey Institute of Technology was supported by NSF grants AGS-1547252 and AGS-1602560. The induction-coil magnetometer project at South Pole is supported by NSF grant OPP-1643700 to New Jersey Institute of Technology. The AAL-PIP array is supported by NSF grant PLR-1543364 to Virginia Tech. Van Allen Probes research at the University of Iowa, University of Minnesota, and Los Alamos National Laboratory was supported by NASA prime contract NAS5-01072 to The Johns Hopkins University Applied Physics Laboratory. We gratefully acknowledge use of NASA/GSFC's Space Physics Data Facility's OMNIWeb, SSCweb, and CDAWeb. MMS CDF data files are publicly available through the MMS Science Data Center at https://lasp.colorado.edu/mms/sdc/public/. IDL routines for display of MMS data are also publicly available in the current SPEDAS software package, which can be found through the MMS Science Data Center and through the THEMIS TDAS website at http://themis.ssl.berkeley.edu/software.shtml. Van Allen Probes CDF data files are available at http://emfisis.physics.uiowa.edu/data/index (EMFISIS) and https://www.rbsp-ect.lanl.gov/science/DataDirectories.php (HOPE). GOES magnetometer data are archived at NOAA's National Centers for Environmental Information (NCEI) http://satdat.ngdc.noaa.gov/sem/goes/data/full/. Spectrograms from the MICA search coil magnetometers at South Pole Station, Antarctica and Sondrestromfjord, Greenland can be accessed at http://space.augsburg.edu/searchcoil/index.html. Spectrograms from the MACCS array magnetometer at Pangnirtung, Canada, can be accessed at http://space.augsburg.edu/maccs/index.html. Spectrograms from the AAL-PIP array search coil magnetometer PG3 can be accessed at http://mist.nianet.org/searchcoil/.

References

Allen, R. C., Zhang, J.-C., Kistler, L. M., Spence, H. E., Lin, R.-L., Dunlop, M. W., & Andre, M. (2013). Multiple bidirectional EMIC waves observed by Cluster at middle magnetic latitudes in the dayside magnetosphere. *Journal of Geophysical Research: Space Physics*, *118*, 6266–6278. https://doi.org/10.1002/jgra.50600

Allen, R. C., Zhang, J.-C., Kistler, L. M., Spence, H. E., Lin, R.-L., Klecker, B., et al. (2015). A statistical study of EMIC waves observed by Cluster: 1. Wave properties. *Journal of Geophysical Research: Space Physics*, *120*, 5574–5592. https://doi.org/10.1002/2015JA021333

Allen, R. C., Zhang, J.-C., Kistler, L. M., Spence, H. E., Lin, R.-L., Klecker, B., et al. (2016). A statistical study of EMIC waves observed by Cluster: 2. Associated plasma conditions. *Journal of Geophysical Research: Space Physics*, *121*, 6458–6479. https://doi.org/10.1002/2016JA022541

Anderson, B. J., Denton, R. E., & Fuselier, S. A. (1996). On determining polarization characteristics of ion cyclotron wave magnetic field fluctuations. *Journal of Geophysical Research*, *101*(A6), 13,195–13,213. https://doi.org/10.1029/96JA00633

Anderson, B. J., Denton, R. E., Ho, G., Hamilton, D. C., Fuselier, S. A., & Strangeway, R. J. (1996). Observational test of local proton cyclotron instability in the Earth's magnetosphere. *Journal of Geophysical Research*, *101*(A10), 21,527–21,543. https://doi.org/10.1029/96JA01251

Anderson, B. J., Erlandson, R. E., Engebretson, M. J., Alford, J., & Arnoldy, R. L. (1996). Source region of 0.2 to 1.0 Hz geomagnetic pulsation bursts. *Geophysical Research Letters*, *23*(7), 769–772. https://doi.org/10.1029/96GL00659

Anderson, B. J., Erlandson, R. E., & Zanetti, L. J. (1992). A statistical study of Pc 1-2 magnetic pulsations in the equatorial magnetosphere 1: Equatorial occurrence distributions. *Journal of Geophysical Research*, *97*(A3), 3075–3088. https://doi.org/10.1029/91JA02706

Anderson, B. J., Fuselier, S. A., Gary, S. P., & Denton, R. E. (1994). Magnetic spectral signatures in the Earth's magnetosheath and plasma depletion layer. *Journal of Geophysical Research*, *99*(A4), 5877–5891. https://doi.org/10.1029/93JA02827

Anderson, B. J., & Hamilton, D. G. (1993). Electromagnetic ion cyclotron waves stimulated by modest magnetospheric compressions. *Journal of Geophysical Research*, *98*(A7), 11,369–11,382. https://doi.org/10.1029/93JA00605

Andriopoulou, M., Nakamura, R., Wellenzohn, S., Torkar, K., Baumjohann, W., Torbert, R. B., & Lindqvist, P.-A. (2018). Plasma density estimates from spacecraft potential using MMS observations in the dayside magnetosphere. *Journal of Geophysical Research: Space Physics*, *123*, 2620–2629. https://doi.org/10.1002/2017JA025086

Arnoldy, R. L., Engebretson, M. J., Alford, J. L., Erlandson, R. E., & Anderson, B. J. (1996). Magnetic impulse events and associated Pc 1 bursts at dayside high latitudes. *Journal of Geophysical Research*, *101*(A4), 7793–7799. https://doi.org/10.1029/95JA03378

Blum, L. W., MacDonald, E. A., Gary, S. P., Thomsen, M. F., & Spence, H. E. (2009). Ion observations from geosynchronous orbit as a proxy for ion cyclotron wave growth during storm times. *Journal of Geophysical Research*, *114*, A10214. https://doi.org/10.1029/2009JA014396

Burch, J. B., Moore, T. E., Torbert, R. B., & Giles, B. L. (2016). Magnetospheric multiscale overview and science objectives. *Space Science Reviews*, *199*(1-4), 5–21. https://doi.org/10.1007/s11214-015-0164-9

Cattell, C., Breneman, A., Colpitts, C., Dombeck, J., Thaller, S., Tian, S., et al. (2017). Dayside response of the magnetosphere to a small shock compression: Van Allen Probes, Magnetospheric MultiScale, and GOES-13. *Geophysical Research Letters*, *44*, 8712–8720. https://doi.org/10.1002/2017GL074895

Chi, P. J., & Russell, C. T. (1998). Phase skipping and Poynting flux of continuous pulsations. *Journal of Geophysical Research*, *103*(A12), 29,479–29,491. https://doi.org/10.1029/98JA02101

Clauer, C. R., Kim, H., Deshpande, K., Xu, Z., Weimer, D., Musko, S., et al. (2014). An autonomous adaptive low-power instrument platform (AAL-PIP) for remote high-latitude geospace data collection. *Geoscientific Instrumentation, Methods and Data Systems*, *3*(2), 211–227. https://doi.org/10.5194/gi-3-211-2014

Cornwall, J. M. (1965). Cyclotron instabilities and electromagnetic emission in the ultra low frequency and very low frequency ranges. *Journal of Geophysical Research*, *70*(1), 61–69. https://doi.org/10.1029/JZ070i001p00061

Cornwall, J. M., Coronoti, F. V., & Thorne, R. M. (1970). Turbulent loss of ring current protons. *Journal of Geophysical Research*, *75*(25), 4699–4709. https://doi.org/10.1029/JA075i025p04699

Denton, R. E., Anderson, B. J., Ho, G., & Hamilton, D. C. (1996). Effects of wave superposition on the polarization of electromagnetic ion cyclotron waves. *Journal of Geophysical Research*, *101*(A11), 24,869–24,885. https://doi.org/10.1029/96JA02251

Denton, R. E., Gary, S. P., Anderson, B. J., Fuselier, S. A., & Hudson, M. K. (1994). Low-frequency magnetic fluctuation spectra in the magnetosheath and plasma depletion layer. *Journal of Geophysical Research*, *99*(A4), 5893–5901. https://doi.org/10.1029/93JA02729

Denton, R. E., Hudson, M. K., Fuselier, S. A., & Anderson, B. J. (1993). Electromagnetic ion cyclotron waves in the plasma depletion layer. *Journal of Geophysical Research*, *98*(A8), 13,477–13,490. https://doi.org/10.1029/93JA00796

Engebretson, M. J., Hughes, W. J., Alford, J. L., Zesta, E., Cahill, L. J. Jr., Arnoldy, R. L., & Reeves, G. D. (1995). Magnetometer array for cusp and cleft studies observations of the spatial extent of broadband ULF magnetic pulsations at cusp/cleft latitudes. *Journal of Geophysical Research*, *100*(A10), 19,371–19,386. https://doi.org/10.1029/95JA00768

Ergun, R. E., Tucker, S., Westfall, J., Goodrich, K. A., Malaspina, D. M., Summers, D., et al. (2016). The spin-plane double probe electric field instrument for MMS. *Space Science Reviews*, *199*(1-4), 167–188. https://doi.org/10.1007/s11214-014-0115-x

Fraser, B. J., & Nguyen, T. S. (2001). Is the plasmapause preferred source region of electromagnetic ion cyclotron waves in the magnetosphere? *Journal of Atmospheric and Solar - Terrestrial Physics*, *63*(11), 1225–1247. https://doi.org/10.1016/S1364-6826(00)00225-X

Funsten, H. O., Skoug, R. M., Guthrie, A. A., MacDonald, E. A., Baldonado, J. R., Harper, R. W., et al. (2013). Helium, Oxygen, Proton, and Electron (HOPE) mass spectrometer for the Radiation Belt Storm Probes Mission. *Space Science Reviews*, *179*(1-4), 423–484. https://doi.org/10.1007/s11214-013-9968-7

Fuselier, S. A., Gary, S. P., Thomsen, M. F., Claflin, E. S., Hubert, B., Sandel, B. R., & Immel, T. (2004). Generation of transient dayside subauroral proton precipitation. *Journal of Geophysical Research*, *109*, A12227. https://doi.org/10.1029/2004JA010393

Fuselier, S. A., Lewis, W. S., Schiff, C., Ergun, R., Burch, J. L., Petrinec, S. M., & Trattner, K. J. (2016). Magnetospheric Multiscale Science Mission profile and operations. *Space Science Reviews*, *199*(1-4), 77–103. https://doi.org/10.1007/s11214-014-0087-x

Gary, P. S., Moldwin, M. B., Thomsen, M. F., Winske, D., & McComas, D. J. (1994). Hot proton anisotropies and cool proton temperatures in the outer magnetosphere. *Journal of Geophysical Research*, *99*(A12), 23,603–23,615. https://doi.org/10.1029/94JA02069

Greifinger, P. (1972a). Ionospheric propagation of oblique hydromagnetic plane waves at micropulsation frequencies. *Journal of Geophysical Research*, *77*(13), 2377–2391. https://doi.org/10.1029/JA077i013p02377

Greifinger, P. (1972b). Micropulsations from a finite source. *Journal of Geophysical Research*, *77*(13), 2392–2396. https://doi.org/10.1029/JA077i013p02392

Hughes, W. J. (1974). The effect of the atmosphere and ionosphere on long period magnetospheric micropulsations. *Planetary and Space Science*, *22*(8), 1157–1172. https://doi.org/10.1016/0032-0633(74)90001-4

Hughes, W. J., & Southwood, D. J. (1976). The screening of micropulsation signals by the atmosphere and ionosphere. *Journal of Geophysical Research*, *81*(19), 3234–3240. https://doi.org/10.1029/JA081i019p03234

Ipavich, F. M., & Scholer, M. (1983). Thermal and suprathermal protons and alpha particles in the Earth's plasma sheet. *Journal of Geophysical Research*, *88*(A1), 150–160. https://doi.org/10.1029/JA088iA01p00150

Keika, K., Takahashi, K., Ukhorskiy, A. Y., & Miyoshi, Y. (2013). Global characteristics of electromagnetic ion cyclotron waves: Occurrence rate and its storm dependence. *Journal of Geophysical Research: Space Physics*, *118*, 4135–4150. https://doi.org/10.1002/jgra.50385

Kennel, C. F., & Petschek, H. E. (1966). Limit on stably trapped particle fluxes. *Journal of Geophysical Research*, *71*(1), 1–28. https://doi.org/10.1029/JZ071i001p00001

Kim, E.-H., & Johnson, J. R. (2016). Full-wave modeling of EMIC waves near the He^+ gyrofrequency. *Geophysical Research Letters*, *43*, 13–21. https://doi.org/10.1002/2015GL066978

Kim, E.-H., Johnson, J. R., Kim, H., & Lee, D.-H. (2015). Inferring magnetospheric heavy ion density using EMIC waves. *Journal of Geophysical Research: Space Physics*, *120*, 6464–6473. https://doi.org/10.1002/2015JA021092

Kim, E.-H., Johnson, J. R., & Lee, D.-H. (2008). Resonant absorption of ULF waves at Mercury's magnetosphere. *Journal of Geophysical Research*, *113*, A11207. https://doi.org/10.1029/2008JA013310

Kim, E.-H., Johnson, R., Lee, D.-H., & Pyo, Y. S. (2013). Field-line resonance structures in Mercury's multi-ion magnetosphere. *Earth, Planets and Space*, *65*(5), 447–451. https://doi.org/10.5047/eps.2012.08.004

Kim, H., Clauer, C. R., Gerrard, A. J., Engebretson, M. J., Hartinger, M. D., Lessard, M. R., et al. (2017). Conjugate observations of electromagnetic ion cyclotron waves associated with traveling convection vortex events. *Journal of Geophysical Research: Space Physics*, *122*, 7336–7352. https://doi.org/10.1002/2017JA024108

Kletzing, C. A., Kurth, W. S., Acuna, M., MacDowall, R. J., Torbert, R. B., Averkamp, T., et al. (2013). The Electric and Magnetic Field Instrument Suite and Integrated Science (EMFISIS) on RBSP. *Space Science Reviews*, *179*(1-4), 127–181. https://doi.org/10.1007/s11214-013-9993-6

Lee, D. H., Johnson, J. R., Kim, K., & Kim, K.-S. (2008). Effects of heavy ions on ULF wave resonances near the equatorial region. *Journal of Geophysical Research*, *113*, A11212. https://doi.org/10.1029/2008JA013088

Lee, J. H., & Angelopoulos, V. (2014). Observations and modeling of EMIC wave properties in the presence of multiple ion species as function of magnetic local time. *Journal of Geophysical Research: Space Physics*, *119*, 8942–8970. https://doi.org/10.1002/2014JA020469

Lin, R.-L., Zhang, J.-C., Allen, R. C., Kistler, L. M., Mouikis, C. G., Gong, J.-C., et al. (2014). Testing linear theory of EMIC waves in the inner magnetosphere: Cluster observations. *Journal of Geophysical Research: Space Physics*, *119*, 1004–1027. https://doi.org/10.1002/2013JA019541

Lindqvist, P.-A., Olsson, G., Torbert, R. B., King, B., Granoff, M., Rau, D., et al. (2016). The spin-plane double probe electric field instrument for MMS. *Space Science Reviews*, *199*(1-4), 137–165. https://doi.org/10.1007/s11214-014-0116-9

Liu, Y. H., Fraser, B. J., & Menk, F. W. (2012). Pc2 EMIC waves generated high off the equator in the dayside outer magnetosphere. *Geophysical Research Letters*, *39*, L17102. https://doi.org/10.1029/2012GL053082

Liu, Y. H., Fraser, B. J., Menk, F. W., Zhang, J.-C., Kistler, L. M., & Dandouras, I. (2013). Correction to "Pc2 EMIC waves generated high off the equator in the dayside outer magnetosphere". *Geophysical Research Letters*, *40*, 1950–1951. https://doi.org/10.1002/grl.50283

Mauk, B. H., Fox, N. J., Kanekal, S. G., Kessel, R. L., Sibeck, D. G., & Ukhorskiy, A. (2013). Science objectives and rationale for the Radiation Belt Storm Probes mission. *Space Science Reviews*, *179*(1-4), 3–27. https://doi.org/10.1007/s11214-012-9908-y

McCollough, J. P., Elkington, S. R., & Baker, D. N. (2012). The role of Shabansky orbits in compression-related electromagnetic ion cyclotron wave growth. *Journal of Geophysical Research*, *117*, A01208. https://doi.org/10.1029/2011JA016948

McCollough, J. P., Elkington, S. R., Usanova, M. E., Mann, I. R., Baker, D. N., & Kale, Z. C. (2010). Physical mechanisms of compressional EMIC wave growth. *Journal of Geophysical Research*, *115*, A10214. https://doi.org/10.1029/2010JA015393

Means, J. D. (1972). Use of the three-dimensional covariance matrix in analyzing the polarization properties of plane waves. *Journal of Geophysical Research*, *77*, 5551–5559. https://doi.org/10.1029/JA077i028p05551

Min, K., Lee, J., Keika, K., & Li, W. (2012). Global distribution of EMIC waves derived from THEMIS observations. *Journal of Geophysical Research*, *117*, A05219. https://doi.org/10.1029/2012JA017515

Noh, S.-J., Lee, D.-Y., Choi, C.-R., Kim, H., & Skoug, R. (2018). Test of ion cyclotron resonance instability using proton distributions obtained from Van Allen Probe-A observations. *Journal of Geophysical Research: Space Physics*, *123*, 6591–6610. https://doi.org/10.1029/2018JA025385

Omura, Y., Pickett, J., Grison, B., Santolík, O., Dandouras, I., Engebretson, M., et al. (2010). Theory and observation of electromagnetic ion cyclotron triggered emissions in the magnetosphere. *Journal of Geophysical Research*, *115*, A07234. https://doi.org/10.1029/2010JA015300

Pickett, J. S., Grison, B., Omura, Y., Engebretson, M. J., Dandouras, I., Masson, A., et al. (2010). Cluster observations of EMIC triggered emissions in association with Pc1 waves near Earth's plasmapause. *Geophysical Research Letters*, *37*, L09104. https://doi.org/10.1029/010GL042648

Remya, B., Lee, K. H., Lee, L. C., & Tsurutani, B. T. (2017). Coherency and ellipticity of electromagnetic ion cyclotron waves: Satellite observations and simulations. *Journal of Geophysical Research: Space Physics*, *122*, 3374–3396. https://doi.org/10.1002/2016JA023588

Russell, C. T., Anderson, B. J., Baumjohann, W., Bromund, K. R., Dearborn, D., Fischer, D., et al. (2016). The Magnetospheric Multiscale Magnetometers. *Space Science Reviews*, *199*(1-4), 189–256. https://doi.org/10.1007/s11214-014-0057-3

Segre, S. E. (1994). Effects of plasma birefringence on the measurement of tokamak safety factor profiles by Faraday rotation. *Plasma Physics and Controlled Fusion*, *36*(5), 715–718. https://doi.org/10.1088/0741-3335/36/5/001

Singer, H. J., Matheson, L., Grubb, R., Newman, A., & Bouwer, S. D. (1996). Monitoring space weather with the GOES magnetometers. In E. R. Washwell (Ed.), *SPIE Conference Proceedings* (Vol. 2812, pp. 299–308). Bellingham, WA: GOES-8 and Beyond SPIE.

Spasojevic, M., Blum, L. W., MacDonald, E. A., Fuselier, S. A., & Golden, D. I. (2011). Correspondence between a plasma-based EMIC wave proxy and subauroral proton precipitation. *Geophysical Research Letters*, *38*, L23102. https://doi.org/10.1029/2011GL049735

Spence, H. E., Reeves, G. D., Baker, D. N., Blake, J. B., Bolton, M., Bourdarie, S., et al. (2013). Science goals and overview of the Energetic Particle, Composition, and Thermal Plasma (ECT) suite on NASA's Radiation Belt Storm Probes (RBSP) Mission. *Space Science Reviews*, *179*, 311–336. https://doi.org/10.1007/s11214-013-0007-5

Tetrick, S. S., Engebretson, M. J., Posch, J. L., Olson, C. N., Smith, C. W., Denton, R. E., et al. (2017). Location of intense electromagnetic ion cyclotron (EMIC) wave events relative to the plasmapause: Van Allen Probes observations, *Journal of Geophysical Research: Space Physics*, *122*, 4064–4088. https://doi.org/10.1002/2016JA023392

Torbert, R. B., Russell, C. T., Magnes, W., Ergun, R. E., Lindqvist, P. A., LeContel, O., et al. (2016). The FIELDS instrument suite on MMS: Scientific objectives, measurements, and data products. *Space Science Reviews*, *199*(1-4), 105–135. https://doi.org/10.1007/s11214-014-0109-8

Usanova, M. E., Mann, I. R., Bortnik, J., Shao, L., & Angelopoulos, V. (2012). THEMIS observations of electromagnetic ion cyclotron wave occurrence: Dependence on AE, SYMH, and solar wind dynamic pressure. *Journal of Geophysical Research*, *117*, A10218. https://doi.org/10.1029/2012JA018049

Usanova, M. E., Mann, I. R., Kale, Z. C., Rae, I. J., Sydora, R. D., Sandanger, M., et al. (2010). Conjugate ground and multisatellite observations of compression-related EMIC Pc1 waves and associated proton precipitation. *Journal of Geophysical Research*, *115*, A07208. https://doi.org/10.1029/2009JA014935

Vines, S. K., Fuselier, S. A., Trattner, K. J., Burch, J. L., Allen, R. C., Petrinec, S. M., et al. (2017). Magnetospheric ion evolution across the low-latitude boundary layer separatrix. *Journal of Geophysical Research: Space Physics*, *122*, 10,247–10,262. https://doi.org/10.1002/2017JA024061

Yahnin, A. G., Popova, T. A., & Yahnina, T. A. (2015). Some characteristics of the magnetospheric source of dayside subaroural proton precipitations during magnetospheric compression. *Cosmic Research*, *53*(1), 80–87. https://doi.org/10.1134/S0010952515010086

Young, D. T., Burch, J. L., Gomez, R. G., de Los Santos, A., Miller, G. P., Wilson, P., et al. (2016). Hot plasma composition analyzer for the Magnetospheric Multiscale mission. *Space Science Reviews*, *199*(1-4), 407–470. https://doi.org/10.1007/s11214-014-0119-6

Yu, X., Yuan, Z., Huang, S., Wang, D., Li, H., Qiao, Z., & Yao, F. (2017). EMIC waves covering wide L shells: MMS and Van Allen Probes observations. *Journal of Geophysical Research: Space Physics*, *122*, 7387–7395. https://doi.org/10.1002/2017JA023982